

CONTROL OF SILVER AND SILICON MICROSTRUCTURE VIA LOW-  
DOSE ION IMPLANTATION

BY LONGXING CHI, B.ENG

A Thesis Submitted to the School of Graduate Studies in Partial Fulfilment of  
Requirements for the Degree Master of Applied Science

McMaster University © Copyright by Longxing Chi, December 2018

MASTER OF APPLIED SCIENCE (2018)

Materials Science and Engineering

McMaster University, Hamilton, Ontario, Canada

TITLE: Control of Silver and Silicon Microstructure via Low-Dose Ion  
Implantation

AUTHOR: Longxing Chi, B. Eng. (Shaanxi University of Science and  
Technology)

SUPERVISOR: Professor Nabil D. Bassim

NUMBER OF PAGES: xii, 68

## **LAY ABSTRACT**

Ag is a critical ohmic contact material in the semiconductor industry. However, agglomeration and dewetting of Ag thin films during thermal processing at medium temperatures annealing inhibits its application and decreases its performance. Here, we introduce an anti-dewetting strategy using ion implantation and successfully suppress 100 nm thick Ag thin films from dewetting upon thermal annealing for more than 24 h. Electron microscopy and thermodynamic simulation are conducted to analyze the anti-dewetting mechanism of this method. Consequently, we successfully interpret the influence of external species on film wettability as well as predict the critical doping concentration necessary to suppress Ag thin film from dewetting and agglomerating upon thermal annealing. Finally, we proposed a novel Si patterning technique by ion implantation followed by thermal annealing which might be useful in semiconductor industries in the future.

## ABSTRACT

Ag thin film dewetting upon high temperature annealing is a non-trivial problem for its application in the semiconductor industry as an ohmic contact metal. Thus, preventing Ag thin film from dewetting is of great importance. Typically, adhesion-promoting layers of chromium are deposited to prevent dewetting, but this deposition has its own process optimization parameters. In this thesis, we introduce an alternative, novel strategy for dewetting prevention via Si or In ion implantation. Electron microscopy including SEM, AFM and AES are conducted to characterize changes in film morphology after ion implantation. Thermodynamic simulation is established to better understand the mechanism of this anti-dewetting approach as well as to predict the performance of doped Ag thin films.

It is found that Ag films implanted by a trace amount of Si dopants remain intact after 24 h annealing at 530°C rather than break down into isolated particles as pure Ag film did. Furthermore, Ag grains in doped samples are much smaller than that in non-doped samples and higher Si or In doses contribute to smaller grains, indicating that a retarding force against film grain growth is introduced by the implanting species. Fortunately, electrical conductivity and optical reflectivity of doped films change trivially, suggesting an insignificant influence of external species on the film performance. The retarding force suppressing film grain growth is demonstrated to be solute drag, which will introduce a size limit towards Ag grain growth. A grain growth model including the solute drag effect is established here to describe the grain growth process. Combining our thermodynamic simulation with our grain growth model in the presence of the solute drag effect, the critical grain diameter to initiate agglomeration of 100 nm thick Ag thin film is calculated to be 350 nm and the critical Si dose to prevent 100 nm thick Ag thin film from dewetting is predicted to be  $2.0 \times 10^{13}$  per  $\text{cm}^2$ .

Finally, we successfully synthesize ultrathin Si thin films via ion implantation and pattern as-deposited Si films by implanting through a hard mask in order to identify some steps towards synthesizing 2-D silicon, or silicene. The as-achieved pattern has an identical shape as that of mask, suggesting Si atoms only diffuse within the implanting regions during thermal annealing. Even though only amorphous Si films are prepared at present, this novel strategy possesses potential to fabricated CMOS-compatible 2-D silicon films for semiconductor industry.

## ACKNOWLEDGEMENTS

This research is fully funded by my supervisor, Professor Nabil D. Bassim. First of all, I must extend my appreciation to Prof. Bassim for his concerns, generosity, kindness, patience and assistance he rendered to me in my research. As a supervisor, he spares no effort in instructing my research work, but never pushes me with unbearable pressure; as a group leader, he performs perfectly in unifying our group members and creating a family-like atmosphere among us. It is the harmonious ambiance established by Prof. Bassim that promotes me to progress during my research career. Of course, my appreciation to Prof. Bassim started from the admission day, it is him who offers me such a great opportunity to conduct research in such an excellent place with so many gifted colleagues. There is an ancient saying in China that *once teacher, always teacher* and no other words are capable of better expressing my feelings at present. Once more, I sincerely appreciate Prof. Bassim for his immeasurable contribution to my research, studying and life.

Second, my colleagues in Bassim Research Group also helped me a lot in the past two years and here I must extend my gratitude to Peng Dong, Weiwei Zhang, Hesham El-Sherif and Sam Norris for their suggestions and assistance in my research. Other colleagues at McMaster including Taoran Wang, Prof. Gu Xu, Shenglong Liang, Prof. Hatem Zurob, Doris Stevanovic, Shahram Ghannad-Tavakoli, James Garrett, Prof. Jose M. Moran-Mirabal, Xiuping Ding and Prof. Lyudmila Goncharova from Western University also helped me a lot in my experiments so please accept my most sincere gratitude here.

Finally, I sincerely appreciate the assistance and care from my family including my parents, my sisters and my brother-in-law, my uncle and aunt, my little nephew and niece. It is them who give me endless happiness and support both mentally and physically. My parents almost exhaust their whole life to raise me up and my senior sister and her husband also play critical roles in mentoring me. Without them my life in Canada must be much more difficult and colorless. Here, thank you so much for your care during all these time and I must try my best to achieve my life goals.

## TABLE OF CONTENTS

LAY ABSTRACT .....	iii
ABSTRACT.....	iv
ACKNOWLEDGEMENTS .....	v
TABLE OF CONTENTS .....	vi
LIST OF FIGURES .....	viii
LIST OF TABLES .....	x
LIST OF ABBREVIATIONS .....	xi
DECLARATION OF ACHIEVEMENT .....	xii
1. INTRODUCTION .....	1
1.1 Solid State Dewetting .....	1
1.1.1 Phenomenology of Thin Film Dewetting.....	1
1.1.2 Conventional Strategies in Thin Film Dewetting Prevention .....	6
1.2 Silver Thin Films .....	9
1.3 Silicon Thin Films.....	12
1.4 Ion Implantation.....	14
1.5 Motivations and Aims .....	17
2. EXPERIMENTS .....	19
2.1 Synthesis of Silver Thin Films.....	19
2.2 Silicon and Indium Implantation .....	19
2.3 Thermal Annealing and Silver Desorption.....	20
2.4 Characterization and Performance Measurement .....	20
3. RESULTS AND DISCUSSIONS .....	23
3.1 Characterization of Silver Thin Films.....	23
3.2 Electrical and Optical Performances of Silicon-Doped Silver Thin Films .....	26
3.3 Silver Grain Growth and Silicon-Induced Solute Drag .....	28
3.3.1 Michel’s Solute Drag Model for Grain Growth Fitting .....	28
3.3.2 Modified Solute Drag Model for Grain Growth Fitting .....	31

3.4 Thermodynamic Simulation of Silver Dewetting .....	35
3.4.1 Dewetting Mechanism and Hexagonal-Cylinder Grain Model .....	35
3.4.2 Total Surface Free Energy Calculation .....	39
3.4.3 Dewetting Simulation along with Grain Growth .....	44
3.5 Silicon Thin Film Synthesis via Ion Implantation .....	49
4. CONCLUSIONS.....	55
REFERENCES .....	57

## LIST OF FIGURES

- Figure 1. Sketch of thin film dewetting during thermal annealing.
- Figure 2. Evolution of thin film dewetting on single crystal substrate.
- Figure 3. Evolution of thin film dewetting on polycrystalline substrate.
- Figure 4. Evolution of PS thin film dewetting on a Si substrate.
- Figure 5. Evolution of thin platinum film dewetting at different temperature with different thickness.
- Figure 6. Dewetting of 20 nm thick AuPt thin films annealing at 500°C with different Pt compositions, a-c) corresponds to a Pt composition of 0, 3.6 wt. % and 8.7 wt. %, respectively.
- Figure 7. Changes in grain size of 20 nm thick AuPt thin films with different Pt composition.
- Figure 8. Dewetting prevention by C60 NPs intercalation between PS thin film and Si substrate.
- Figure 9. Illustration of ion implantation machine.
- Figure 10. The illustration of the implantation-assisted silicene synthesis process.
- Figure 11. Ion distribution of Si (a) and In (b) dopants with 100 nm thick Ag thin films simulated by SRIM software.
- Figure 12. Illustration of line intercept method for grain size calculation.
- Figure 13. Illustration of van der Pauw four-point method for electrical resistivity measurement.
- Figure 14. Optical microscopy images of doped and non-doped Ag thin films before and after annealing.
- Figure 15. AFM images of pure Ag (a), Si-doped Ag (b) and In-doped Ag (c) thin films before and after annealing.
- Figure 16. AFM images of Si-doped Ag thin films with different Si dose at different annealing time.
- Figure 17. AFM images of In-doped Ag thin films with an In dose of 1014 ions per cm<sup>2</sup> (a) and 1015 ions per cm<sup>2</sup> (b), respectively after 30 min anneal.
- Figure 18. AES spectra for Si-doped Ag thin film where a) is the depth profile of Si spectrum and b) is the calculated Si atomic percentage along depth.
- Figure 19. Electrical resistivity (a) and optical reflectivity (b) of Ag thin films varying in Si implanting fluences.
- Figure 20. Average grain size of Ag thin films as a function of a) Si implanting dose and b) thermal annealing time based on Michel's solute drag model.
- Figure 21. Average grain size of Ag thin films as a function of a) Si implanting

dose and b) thermal annealing time based on our modified solute drag model.

Figure 22. Different phases during dewetting of Ag thin films.

Figure 23. AFM image of a dewetted Ag film which includes all three dewetting phases.

Figure 24. 2D illustration of different phases during thin film dewetting.

Figure 25. 3D illustration of different phases during thin film dewetting.

Figure 26. Illustration of interface energy in equilibrium.

Figure 27. Illustration of grain in initial film.

Figure 28. Illustration of grain in phase I: continuous film.

Figure 29. Illustration of grain in phase II: porous film.

Figure 30. Illustration of grain in phase III: discrete islands.

Figure 31. AFM images of the edge of our Ag thin film.

Figure 32. Normalized energy distribution as a function of wetting angle  $\theta$  of pure Ag film before and after annealing.

Figure 33. Energy distribution of Ag thin films doped by different dose of Si after 24 h thermal annealing.

Figure 34. Phase diagram of film-substrate system.

Figure 35. Critical dewetting size in the limiting grain size curve calculated from our modified solute drag model.

Figure 36. Illustration of patterned Si thin film synthesis by ion implantation.

Figure 37. Vapor pressure of most common elements.

Figure 38. SEM images of patterned Si thin films.

Figure 39. RBS images of as-prepared Si patterns.

Figure 40. AFM images of Si thin film grains.

Figure 41. TEM and EELS images of Si/sapphire cross section.

## **LIST OF TABLES**

Table 1. SRIM simulation of Si and In implanting into Ag at 30 keV.

Table 2. Si atomic percentage in Ag thin film along depth.

Table 3. Electrical resistivity of Ag thin films doped by different amount of Si.

Table 4. Measured average grain size of Si-doped Ag thin films for different doping fluence at different annealing time.

Table 5. Limiting grain size fitting from our experimental data via equation (10).

Table 6. Limiting grain size fitting from our experimental data via equation (15).

Table 7. Error comparison for Michel's model and our modified model in limiting size simulation.

Table 8. Interface area of grains in initial film.

Table 9. Interface area of grains in phase I.

Table 10. Interface area of grains in phase II.

Table 11. Interface area of grains in phase III.

## **LIST OF ABBREVIATIONS**

Field-effect-transistor – FET.  
Polystyrene – PS.  
Poly-methylmethacrylate – PMMA.  
Poly(4-vinylpyridine) - P4VP.  
Perfluoropolyether – PFPE.  
Poly-ethylenepropylene – PEP.  
Nanoparticles – NP.  
standard cubic centimeter per minute – sccm.  
Scanning electron microscopy – SEM.  
Auger electron spectroscopy – AES.  
Atomic force microscopy – AFM.  
Transmission electron microscopy – TEM.  
Molecular beam epitaxy – MBE.  
Rutherford backscattering spectroscopy – RBS.  
Power conversion efficiency – PCE.  
Density functional theory – DFT.  
Quantum spin hall effect – QSHE.  
Quantum anomalous hall effect – QAHE.  
Two-dimensional – 2D.  
Three-dimensional – 3D.  
Diameter-to-height ratio – D/h.

## **DECLARATION OF ACHIEVEMENT**

Hereby I declare the following contribution in this thesis achieved by either myself, my colleagues or other faculties:

1. **INTRODUCTION:** all writing work was performed by the author and all citations indicate the source material.
2. **EXPERIMENTS:** SRIM simulation was conducted by the author; Ag thin film sputtering was done by the author in McMaster Center for Emerging Device Technology; ion implantation was operated by Doris Stevanovic at McMaster Center for Emerging Device Technology; isothermal annealing was performed by the author in McMaster X-Ray Laboratory. SEM was done by the author in Canadian Center for Electron Microscopy; AFM was done by the author in McMaster Bio-interface Institute; AES was done by Travis Casagrande in Canadian Center for Electron Microscopy; TEM was done by Natalie Hamada in Canadian Center for Electron Microscopy; RBS was done by Lyudmila Goncharova in Western University. Ag grain size measurement was performed by the author; electrical resistivity was measured by the author in Dr. Jose M. Moran-Mirabal's laboratory; optical reflectivity was measured by the author in McMaster Center for Emerging Device Technology.
3. **RESULTS AND DISCUSSIONS:** all writing work and figures were performed and plotted by the author.
4. **CONCLUSIONS:** all writing work was performed by the author.

## 1. INTRODUCTION

### 1.1 Solid State Dewetting

#### 1.1.1 Phenomenology of Thin Film Dewetting

Thin film dewetting under thermal annealing is quite a conventional phenomenon that has been observed in a variety of materials including metals, semiconductors and polymers. In general, solid state dewetting initiates at a grain boundary or a defect region such as surface impurities, grooves and holes, at a temperature below the material melting point. Then, the original continuous film agglomerates into discrete clusters, as shown in Figure 1. The driving force of dewetting originates from the driving force of the film surface and interfaces to minimize their total surface free energy during thermal processing. Solid state dewetting can play a negative role in semiconductor processing, but may play a contributing role in nano-fabrication for self-assembly and is one of the most attractive topics among thin film research.[1-3]

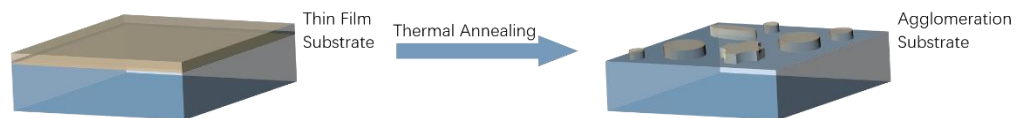


Figure 1. Sketch of thin film dewetting during thermal annealing.

Damage introduced by solid state dewetting during thin film thermal annealing have already been reported in electronic materials.[4-12] Shili Zhang et al. research the dewetting problem of metal silicides, including  $\text{TiSi}_2$ ,  $\text{CoSi}_2$  and  $\text{NiSi}$ , in complementary metal-oxide-semiconductor field-effect-transistor (CMOSFET) where metal silicide thin films perform as conductive contacts between Si substrates and metal electrodes. It was shown that changes in contact morphology significantly influence the device performance and lifetime.[4] In their research, 20 to 100 nm thick metal silicide thin films depositing on the Si wafer substrates are annealed under  $800^\circ\text{C}$  to induce film grain growth. However, dewetting occurs instead and exhibits two different dewetting morphologies according to the crystal structure of the substrates. For single crystal Si substrates, film agglomeration happens with characteristics of surface coarsening and grain boundary grooving so that the total surface free energy of the film is minimized. Such a mechanism, proposed by T. P. Nolan et al., is schematically illustrated in Figure 2 where Figure 2a represents the initial continuous film before annealing with uniform grain size as well as a flat surface and interface; however, along with grain growth, the film grains split at boundaries and spherize upon surfaces (2b-c) until reaching the critical size  $L_c$  (2d). Consequently, grains completely separate from each other and form into discrete islands.[7]

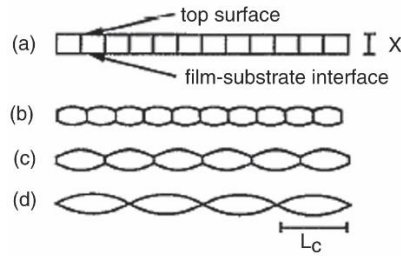


Figure 2. Evolution of thin film dewetting on single crystal substrate.[7]

As for polycrystalline Si substrates, as shown in Figure 3, grains in the film and the substrate grow simultaneously, coarsening at the film-substrate interface. Then the overlayer silicide and sublayer Si wafer incorporate and eventually dewetting happens among grains.[11]

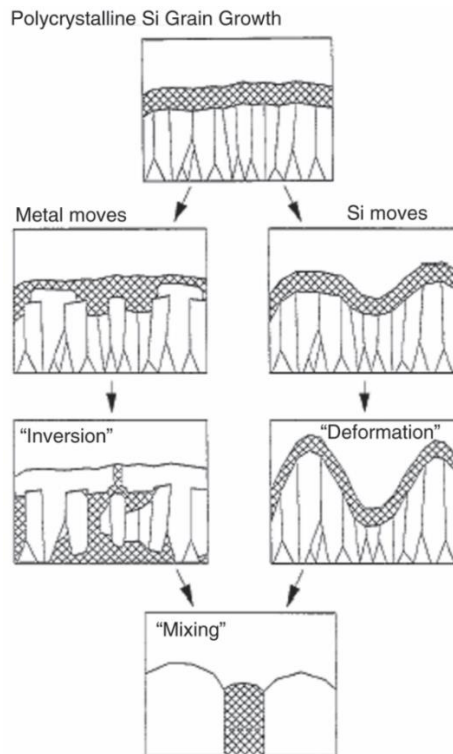


Figure 3. Evolution of thin film dewetting on polycrystalline substrate.[11]

Dewetting also inhibits the application of polymer thin films that are extensively applied in optoelectronics, biotechnology, nanolithography, sensors and actuators, microfluidics, functional coatings and lubricants. Much research into dewetting of polymers is critical to enable their application.[13-24] Dewetting has been investigated upon a variety of polymers such as polystyrene (PS) (the most frequently researched), polymethylmethacrylate (PMMA), poly(4-vinylpyridine) (P4VP), perfluoropolyether (PFPE) and poly-ethylenepropylene (PEP), etc. on slippery substrates including

sapphire, glass, quartz and Si wafers.[17] There are several factors capable of initiating polymer disintegration among which thermal annealing is the most common one. R. Xie et al. published the first paper regarding spinodal dewetting in 1998 in which a 4.5 nm thick PS film deposited on a Si substrate is annealed at 115°C, a temperature beyond its glass transition temperature ( $T_G$ ). Upon annealing, equal-sized circular holes appear upon the PS surface. Dewetting is increased with further annealing.[18] More specifically, as illustrated in Figure 4, holes randomly appear on the polymer surface (4a) and expand gradually with time until reaching the adjacent holes, incorporating into each other and evolving into a network (4b); such a hole network ruins the continuity of the polymer film, breaking it down into isolated patches (4c). The circular holes themselves originate from the rim of other pre-formed holes, as shown in Figure 4d, due to Rayleigh-Plateau instability. The hole rim is extremely unstable and enables the formation of undulating fingers upon the polymer film thus directly leading to the rupture of the film, also known as slippage, as well as the appearance of new holes.

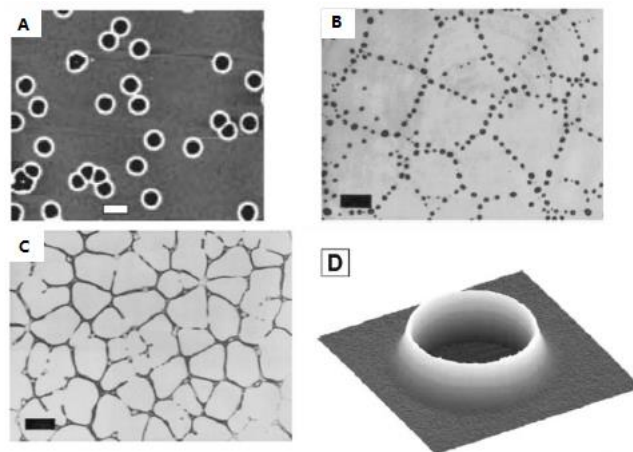


Figure 4. Evolution of PS thin film dewetting on a Si substrate.[18]

Other factors, such as external electric field, thermal gradient and interface interaction also result in the aggregation of polymer thin films but are not introduced here in detail.[13-24]

Dewetting upon thermal annealing also exists in metallic thin films including Ag, Au, Cu, Al, Ti and Pt, which poses nonnegligible threats to their optical, thermal and electrical performances.[25-49] For example, Pt is widely used as temperature sensor, heater and gas sensor in integrated microreactors, which requires a high temperature working environment varying from 500°C to 900°C; however, nanograin agglomeration of Pt thin films starts at ~700°C then increases gradually with an increase in temperature.[33] Figure 5 exhibits dewetting of Pt thin films at different temperatures with different film thickness and it is obvious that higher temperature and thinner films give rise to more severe agglomeration.[33]

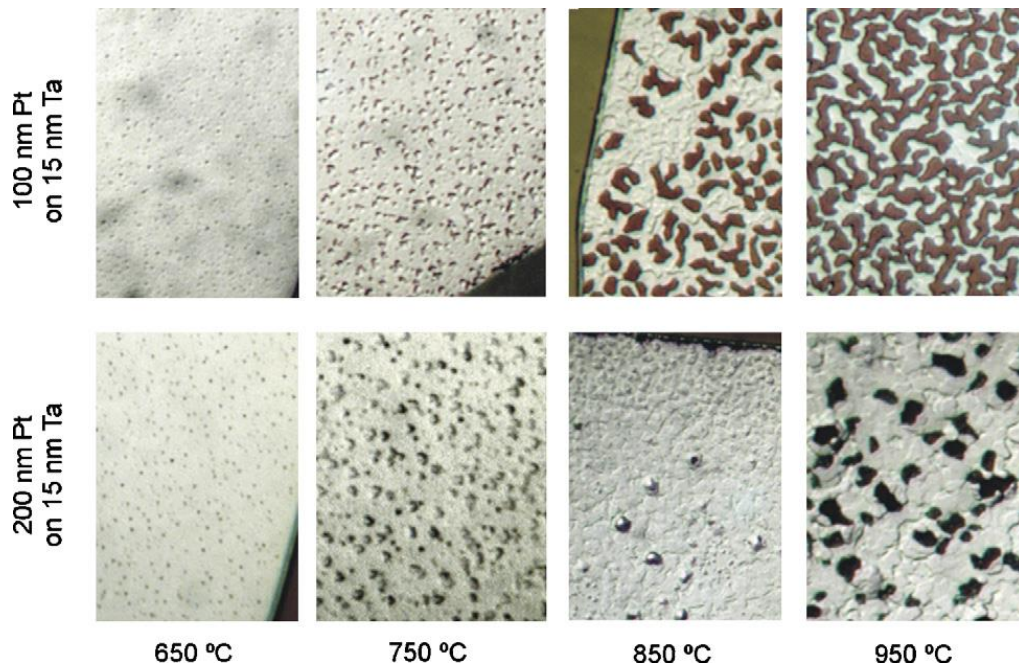


Figure 5. Evolution of thin platinum film dewetting at different temperature with different thickness.[33]

Alloys also suffers from annealing-induced thin film dewetting. For example, FePt, an excellent magnetic alloy being used for magnetic recording media due to its high thermal stability, strong perpendicular magnetic anisotropy (PMA) and writability, alters its wettability when being annealed at 900°C in order to obtain the required anisotropic crystal orientation.[37] Another widely researched alloy AuPt, a typical material used in fuel cells, optical and microelectronic devices, also tends to bead upon annealing and the dewetting rate is largely influenced by the Pt composition within the film.[29] Figure 6 exhibits the dewetting process of three 20 nm thick AuPt thin films annealing at 500°C with a Pt composition of 0 (a), 3.6 wt. % (b) and 8.7 wt. % (c), respectively. It is obvious that the film stabilizes longer with the increase in Pt percentage, indicating a resistance in film dewetting introduced by Pt atoms.[29]

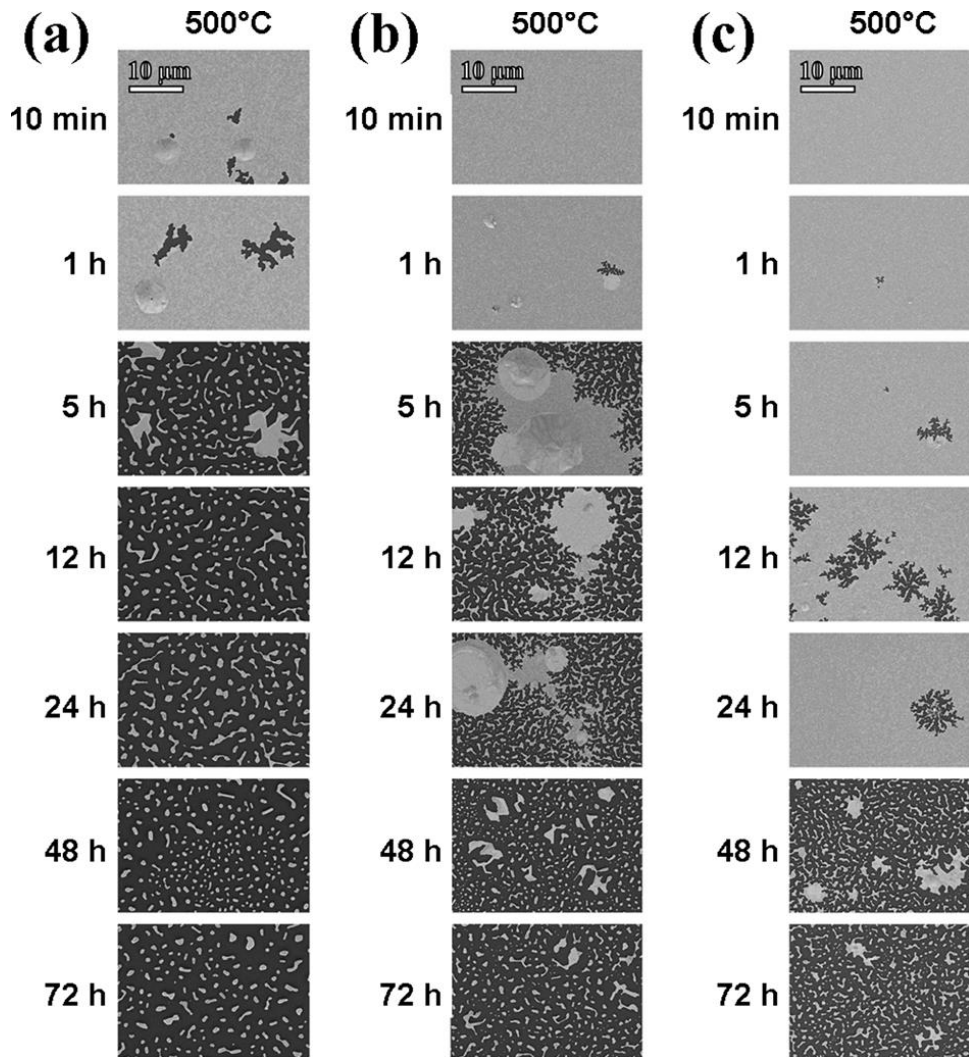


Figure 6. Dewetting of 20 nm thick AuPt thin films annealing at 500°C with different Pt compositions, a-c) corresponds to a Pt composition of 0, 3.6 wt. % and 8.7 wt. %, respectively.[29]

Changes in Pt composition not only preserves the film integrity but also influences the film grain size during grain growth. Figure 7 reveals changes in grain size of 20 nm thick AuPt films with different Pt compositions and it is evident that increasing the Pt proportion substantially inhibits the film grain growth. Indeed, limiting grain size contributes to dewetting suppression to a large extent according to thin film thermodynamics that will be introduced later in this thesis in detail.

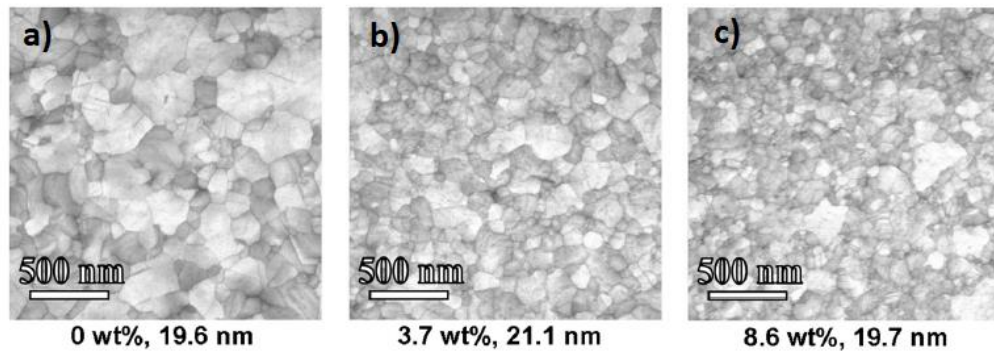


Figure 7. Changes in grain size of 20 nm thick AuPt thin films with different Pt composition.[29]

To summarize, typical examples for thin film dewetting are introduced here including semiconductors, polymers, metals and alloys. Dewetting is a common phenomenon among solid thin films and significantly restricts their applications, therefore, developing effective strategies to prevent thin film dewetting is of great importance in solid state thin film research.

### 1.1.2 Conventional Strategies in Thin Film Dewetting Prevention

Conventional anti-dewetting strategies can be classified into three major categories: 1) interface intercalation, 2) capping layer protection and 3) external doping. In principle, all three methods achieve anti-dewetting via minimizing the total surface free energy of the film grains to make a smooth continuous film energetically-favorable. For interface intercalation, an additional intercalating layer must possess a lower interface energy with the substrate compared to the original film so that the film stabilizes longer than without intercalation; for capping layer protection, the film-substrate interface in this case remains unchanged in spite of the presence of a protective overlayer. Usually the capping layer possesses superior mechanical strength, which is required to suppress film fluctuation and to eliminate surface nonconformity (two major factors accounting for thin film dewetting); for external doping, dopants tend to segregate to the film grain boundaries, grooves and hole sites therefore not only introduce a pinning force against film grain growth but also decrease the film tensile stress that usually results in the film fluctuation and slippage.

Interface intercalation is quite an effective approach in polymer anti-dewetting. For example, S. Roy et al. successfully prevent polystyrene (PS) thin films, grown on single crystal Si substrates, from dewetting via intercalation of C<sub>60</sub> nanoparticles (NP).[14] In their experiments, 112 nm thick PS films are prepared by spin coating, prior to which 0 to 3 wt. % NPs are added into the polymer solutions. Then, as-prepared films are

annealed at 130°C for 46 hours before characterization. The result is illustrated in Figure 8 where different regimes can be found according to the concentration of NPs ( $C_{NP}$ ) (one of the critical parameters to control film wettability). In regime 1 where  $C_{NP} < 0.2\%$ , inclusion of NPs is insufficient to prevent beading of the film because even though the NPs diffuse towards the interface, their content is still too low to fully cover the interface. In regime 2 where  $0.3\% < C_{NP} < 0.75\%$ , dewetting is partially suppressed due to the formation of localized  $C_{60}$  intercalating layers. In regime 3 where  $C_{NP} > 1\%$ , NPs are sufficient to thoroughly saturate the film/substrate interface thereby preventing the film from break down successfully. It is noteworthy that in order to form the intercalating layer, the surface free energy of NPs, i.e.  $C_{60}$  here, must be lower than that of the substrates, i.e. Si in this experiment.

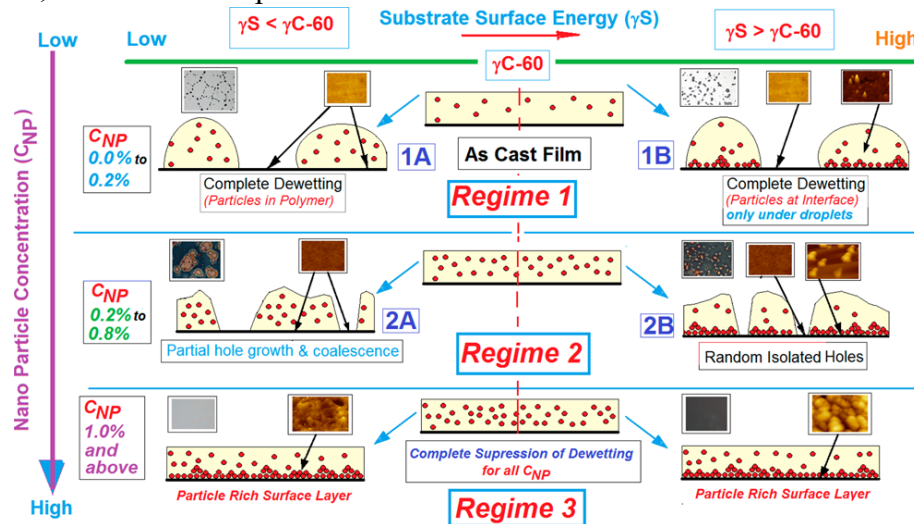


Figure 8. Dewetting prevention by  $C_{60}$  NPs intercalation between PS thin film and Si substrate.[14]

N. Pangpaiboon et al. also suppressed PS thin films from dewetting by mixing  $TiO_2$  NPs into the film.[16] Similar to the function of  $C_{60}$  NPs,  $TiO_2$  NPs prevent film aggregation by distributing diffusing to and remaining at the polymer-substrate interface thereby significantly increasing the surface roughness as well as the wettability of the substrate. Again, the film lifetime is dependent on the concentration of  $TiO_2$  NPs in the rule that higher  $TiO_2$  concentration results in longer film lifetime.

Using capping layers to cover a thin film is another universal anti-dewetting strategy and has been applied in both metallic and polymeric thin film materials. In principle, materials for that purpose must possess strong mechanical strength to inhibit the original film from undulation. For example, P. Cao et al. utilize monolayer graphene and  $MoS_2$  as capping layers to prevent Au and PS thin films from dewetting during annealing, respectively.[32] In detail, monolayer graphene successfully suppresses beading of 20 nm thick gold thin films deposited on  $SiO_2$  substrates followed by 350°C annealing for

4 h; and monolayer MoS<sub>2</sub> successfully restrains break up of 5 to 60 nm thick PS films spin-coated on SiO<sub>2</sub> substrates followed by 180°C annealing for 300 s. According to Cao's thermodynamic simulation, graphene and MoS<sub>2</sub>, with a Young's modulus of 4 TPa and 330 GPa, respectively, are predicted to be strong enough to prevent film fluctuation and to maintain surface conformity as capping layers; furthermore, increasing the Young's modulus of the capping layer enables both the metallic and polymer thin films to stabilize with bigger film grains, at higher annealing temperatures and with lower film thickness.[32] Metals such as Ag can also be used as capping layers to suppress thermally-induced thin film dewetting. S. N. Hsiao et al. deposit 1 to 7 nm thick Ag capping layers upon 10 nm thick FePt thin films during 800°C annealing and successfully stabilize the film.[37] The deposited Ag layer maintains or even enhances the in-plane tensile stress, the resultant (001) texture and the perpendicular anisotropy of the FePt film. Besides, Ag atoms diffusing into the FePt layer significantly promotes its L1<sub>0</sub> ordering.

Besides the interface intercalation and capping layer protection strategies introduced above, one emerging anti-dewetting strategy, known as external doping, has been reported by several research groups in different film-substrate systems and is now attracting more and more attention. Doping-induced dewetting suppression was first reported by R. E. Hummel et al.[31] In his paper, trace amounts of Na and In atoms are doped into 80 nm thick Au thin films, via vapor deposition, followed by thermal annealing at different temperatures. It was found that In atoms successfully prohibit Au films from rupture at all experimental annealing temperatures while Na atoms fail to achieve this goal; In or Na interlayers between Au film and substrate that might be generated during annealing due to atomic diffusion is not detected by electron diffraction, indicating that external doping follows a completely different anti-dewetting mechanism than that of interface intercalation. At that point, no thermodynamic interpretation regarding this phenomenon or an explanation of the differing behaviors of Na and In atoms resulting in different film morphologies upon thermal annealing were offered. Similar research was done later in 2008 by J. H. Son et al. where they precipitate Cu<sub>2</sub>O into 150 nm thick Ag thin film to prevent it from aggregation. The mechanism is interpreted by that Cu<sub>2</sub>O precipitation segregates to Ag grain boundaries thereby preventing the Ag grain growth and film aggregation.[34] Cu<sub>2</sub>O in this case is deposited onto Ag by electron beam evaporation and uses thermal annealing to enable a uniform distribution of Cu<sub>2</sub>O inside the Ag film. External doping also applies to photonic materials: it is known that Ag is an excellent plasmonic material under visible and near infrared light due to its high conductivity and low optical loss under visible and infrared range. However, thermal-induced dewetting severely restricts its usage in photonic devices. Fortunately, C. Zhang et al. solve this problem in virtue of external doping of Al atoms.[25, 26, 45] In their experiments, sputtering is used for

Al doping and to ensure the uniform distribution of Al dopants within a 10 nm thick Ag film, two sputter guns with different depositing rate are operated simultaneously in the vacuum chamber, i.e. cosputtering, during film deposition with one of which loaded by Ag while another Al. The result shows that 1) film agglomeration disappears completely in Al-doped Ag films, 2) a much lower surface roughness than pure Ag film is achieved and 3) optical performance of the Ag film, such as optical permittivity and transmittance, changes trivially after Al doping, all of which fully demonstrate the superiority of this Al-doping strategy in anti-dewetting. However, again none of the abovementioned researchers offer a reasonable thermodynamic interpretation to the doping-induced anti-dewetting. Therefore, further research is still required to better explain this phenomenon.

In summary, three major strategies of thin film dewetting prevention are introduced here, i.e. interface intercalation, capping layer protection and external doping, with several successful examples for each method. It is clear that all three strategies, no matter how it works eventually, eliminate film dewetting by minimizing the total surface free energy of the target film. Nevertheless, more fundamental research is necessary to elucidate the mechanism of thin film dewetting prevention.

## 1.2 Silver Thin Films

Ag is the 47<sup>th</sup> element in periodic table with an outmost electron configuration of  $4d^{10}5s^1$ , similar to that of Cu ( $3d^{10}4s^1$ ) and Au ( $5d^{10}6s^1$ ). Such a half occupied outmost shell along with a fully occupied d subshell gives rise to many particular properties in Ag. Ag is a pretty soft, ductile and malleable transition metal with face-centered cubic lattice. Its outmost single 5s electron is delocalized, being able to move free of bond restrictions. Therefore, electrons from the 5s orbital in Ag consist of the “electron gas” within the metal that accounts for the high electrical conductivity of Ag. Ag is a popular choice for reflective Ohmic contact material, plasmonic devices as well as some optoelectronics usage due to its excellent light reflectance (~95%) in the visible range, extremely low contact resistivity in an order of  $10^{-8} \Omega \cdot m$  and superior thermal stability.[34, 36] Ag is usually processed to nanoscale thin film geometries for applications in both p-Ohmic contact and optoelectronic devices. Annealing is critical during device assembling because that 1) Ag grains are allowed to grow under high temperature thereby contributing to a better crystalline structure of Ag film as well as to a better film performance and 2) it is critical to remove physical interface between Ag contact layer and device body, while annealing is an efficient method to promote chemical bonding between Ag layer and adjacent device layer. Therefore, the poor adhesion of Ag on substrate during thermal annealing becomes one of the biggest obstructions for its utilization; also, seeking an effective approach to solve Ag agglomeration is of great significance.

Film evolution models ought to consider that Ag thin films experience grain growth and dewetting simultaneously during thermal annealing and they are expected to be closely related to each other according to our current research. Ag grain growth follows the Volmer-Weber model where deposited atoms first nucleate into small separated islands then further expand and coalesce into a porous film with incoherent grain boundaries.[50] The final morphology of Ag and whether it evolves into continuous film or stays as a semi-connected film, is controlled by the film thickness. To form a continuous film, Ag must exceed a height threshold, usually between 10 to 20 nm, in order to eliminate internal film porosity. For Ag thin films thicker than the threshold, grain growth can be described kinetically. In this description, the growth rate is proportional to the curvature of grain radius:

$$\frac{dD(t)}{dt} = \frac{A}{D} \quad (1)$$

where  $t$ ,  $D(t)$  and  $A$  represent the annealing time, average Ag grain size at time  $t$  and a mobility-related coefficient, respectively.[51-53] Annealing temperature is a critical factor during Ag grain growth and its influence is incorporated into the equation coefficient  $A$ . Solving equation (1) enables us to derive the grain growth equation with regard to annealing time under ideal conditions:

$$D(t)^2 - D_0^2 = A \cdot t \quad (2)$$

where the new term  $D_0$  is the initial average grain size before annealing and can be easily measured using electron microscopy or atomic force microscopy. Equation (2) suggests a parabolic tendency for Ag grain growth, however, it is worth mentioning that this equation only applies to ideal conditions ignoring the influence of impurities, surface fluctuations, surface oxidation and even film agglomeration. The true grain growth kinetics can be much more complicated and obstructing factors resulted from impurities or other barriers should be taken into account according to the real-world circumstances. This model was proposed by J. E. Bruker in 1949 and has been demonstrated on many other metallic systems including Au, Cu, Fe over the last few decades.[51-77]

Ag grain growth in the presence of impurities also deserves attention and different kinds of impurities lead to different grain growth modes for Ag thin films. Hindrance introduced by second-phase NPs is known as Zener drag and has been reported in several noneutectic two-phase metallic systems.[67, 78-80] Generally speaking, grain growth is driven by grain boundary motion. When a grain boundary encounters an impurity NP, a new interface is generated between grain boundaries and the particle surface and in order to minimize the interface energy a pinning force against grain growth initiates. In equilibrium, the driving force for grain growth is identical to the pinning force for boundary motion, indicating the termination of boundary motion as

well as grain growth. In other words, grain growth reaches a size limit due to Zener drag at equilibrium. The limiting size is dependent on both particle size and particle volume fraction in a relationship of:

$$R_c = k \cdot \frac{r}{f^m} \quad (3)$$

where  $R_c$ ,  $k$ ,  $r$  and  $f$  represent the limiting radius of Ag, a temperature-dependent coefficient, the average radius of external particles and their volume fraction within the Ag film, respectively. The index  $m$  here is an empirical value, obtained from previous databases, that can either be a fraction or an integer varying with the film-substrate system.

Another universal impurity existing in Ag crystals is solute atoms that introduces solute drag against Ag grain growth within the film. Solute atoms do not self-assemble into particles, but instead, they tend to segregate at grain boundaries as solute atoms. A retarding force on grain boundary migration, i.e. solute drag, is attributed to the concentration difference between of solute atoms inside grains and at grain boundaries. Interestingly, the influence of solute drag varies widely among different crystal structures. For example, solute drag in bulk Fe, as reported by H. S. Zurob et al. showed the influence of tiny amount of carbon solute atoms, from 0.006% to 0.06%, in polycrystalline Fe bulks. The carbon slows down the Fe grain growth to a large extent but never completely stops it from growing. In other words, no grain size limit exists in this case.[55] However, a completely different phenomenon in nanocrystalline thin films is observed in which grain growth stops at a limiting grain size within nanocrystal range. For example, A. Michels et al. prepare nanocrystalline Pd<sub>81</sub>Zr<sub>19</sub> using mechanical alloying at an annealing temperature of 600°C and they find that a grain size limit of approximate 16 nm for grain growth reaches after 10 h annealing[59]. In this case, solute drag is dependent on both the solute concentration and on the average film grain size. It is quite challenging to generalize the abovementioned contradictory studies into a unifying theory as each case is interpreted separately based on different models. In our experiments, Ag film is doped by a trace amount of Si or In atoms and after 5 h thermal annealing, Ag grain growth terminates at an average grain diameter between tens and hundreds nanometers, which is quite consistent to that of Michels' results. These will be discussed in greater detail later in this document.

Overall, properties, applications and grain growth mechanisms of Ag are briefly introduced in this section. As is known, Ag is widely used as Ohmic contact and plasmonic material due to its excellent contact conductivity, reflectivity at visible range and thermal stability. Ag is usually applied in the form of nanoscale thin films. Thus, solving the dewetting problem of Ag thin film is critical.

### 1.3 Silicon Thin Films

Si is the 14<sup>th</sup> element in the periodic table with four outmost electrons ( $3s^23p^2$ ) and this unique electron configuration gives rise to extraordinary electrical properties of Si. In Si crystal, the four outmost electrons in one atom form  $sp^3$  hybrid orbitals and bond with electrons from neighboring Si atoms. Therefore, Si crystals exhibit a diamond-like crystalline structure with each atom bonding with another three atoms to form a tetrahedral unit cell. Si is highly thermally stable with a melting point of 1414°C: the second highest value among metalloids and nonmetals (just below B whose melting point is 2076°C). Si is also the second most abundant element in the Earth's crust (around 28% after oxygen) and exists in the form of silicate minerals exploiting from sands, stones, earth and so on. Besides, Si is also the eighth most common element in the universe widely distributing among dusts, planetoids and planets. The abundance of silicate minerals makes it an economical candidate for industrial use and, accordingly, the Si industry dominated the electronics market for decades due to its excellent performance, stability and price. It is worth mentioning that pure Si can hardly be found in nature therefore preparing high quality Si from silicate and oxide minerals is a thriving industry at present as well.

Si is a group IV semiconductor material with a bandgap of 1.1 eV, which enables its broad application in transistors, solar cells and integrated circuits. With the help of doping technology, extrinsic charge carriers are introduced into Si thereby significantly improving its electrical conductivity. Moreover, different types of dopants also introduce different charge carriers. Si doped by group V elements, e.g. P, contains extra free electrons because each P atom bonding with four Si atoms releases one free electron. In contrast, Si doped by group III elements, e.g. B, possess additional free holes considering every B atom connecting with other four Si atoms leaves one hollow orbital without hybridization. Si containing extra free electrons is known as n-type semiconductor with n referring to negative; while Si including extrinsic free holes is known as p-type semiconductor with p referring to positive. Interface between p-type and n-type semiconductor is defined as p-n junction, which contributes to the peculiarity of diodes, transistors, solar cells and other semiconductor devices. P-n junction generates a depletion region at p-n interface whose performance is dominated by two typical mechanisms, i.e. diffusion and drifting. Diffusion originates from concentration difference of charge carriers between each side of the p-n junction and obviously electrons diffuse from n side to p side while holes diffuse in the opposite direction. Drifting results from the electric field generated from within the depletion region, which allows electrons and holes to drift in response to an electric field. Diffusion and drifting generate diffusion current and drift current, respectively, and two currents balance each other until reaching equilibrium. Consequently, there is no net current flowing within

the p-n junction in the meanwhile an internal bias forms between p-type and n-type Si. P-n junctions are directly used in solar cells via exposing under light to generate excitons and in diodes by imposing either a forward or backward bias to the junction. Other than p-n junctions, doping technology also enables formation of p-n-p and n-p-n structures in one Si wafer thus a bipolar transistor is built which can be used for amplifiers, modulators and rectifiers, etc. More sophisticated Si-based devices include field-effect transistors, or FETs.

Si thin films then should be emphasized considering the trend of shrinking device dimensions in the semiconductor industry. For example, thin film Si solar cells are one of the evolutions of traditional macroscale Si solar cells. Thin films used for solar cells no longer come from Si wafer but from either physical or chemical deposition techniques such as Molecular Beam Epitaxy (MBE), e-beam evaporation, vacuum sputtering, chemical intercalation, or other techniques. Film height for solar-cell application is usually controlled to be hundreds of nanometers and crystalline films, especially single crystal, provide higher power conversion efficiency (PCE) than amorphous Si films.[81-98] Therefore, it is critical to develop technologies capable of preparing high quality crystalline Si thin films; furthermore, potential techniques must be economical for commercial use. When the film thickness shrinks to the atomic scale, like single or few monolayers, the silicon films start to exhibit quantum features, such as Quantum Spin Hall Effect (QSHE), Quantum Anomalous Hall Effect (QAHE) and topological properties.[99, 100] Monolayer silicon is especially designated as silicene, which was first synthesized upon a Ag(111) film by Guy Le Lay et al. in 2011 using e-beam evaporation.[101] The peculiarity of silicene differentiating from bulk Si is that the band structure of silicene at Fermi level exhibits a Dirac cone, just like its C analogue graphene, making silicene another semi-metal.[101] Furthermore, QSHE is predicted to exist in silicene thereby opening a tiny bandgap of 1.55 meV at its Dirac cone near Fermi level. Free standing silicene is proved to be energy unfavorable based on the Density Functional Theory (DFT) calculations conducted by Junfeng Gao et al in 2012, therefore, silicene requires specific substrates for its growth.[102] Until now silicene has been successfully prepared on Ag(111), Ir(111), Ru(0001), ZrB<sub>2</sub>(0001), graphite, MoS<sub>2</sub>, ZrC(111) and SiC(0001) by either MBE, chemical intercalation or e-beam evaporation.[101, 103-141] Qualified substrates for silicene growth must consist of hexagonal lattice with small lattice mismatch to silicene. Other than aforementioned methods in silicene synthesis, ion implantation, chemical exfoliation, surface etching, sonication and centrifugation are also effective ways in silicene preparation, which are not introduced here in further detail.[142-150] In spite of the above contributions done by previous researchers, more challenges are still waiting to be overcome in order to get high quality silicene, including dealing with oxidation, surface contamination, strong substrate bonding, fluctuation and aggregation, among other issues.

Among all the above synthesizing techniques, vapor pressure is a determining parameter. Vapor pressure is the pressure of an equilibrium vapor phase at a given temperature and in a closed system, which indicates the liquid evaporation rate at the given temperature. Vapor pressure of pure materials can be estimated by the Antoine equation and the vapor pressure of most common elements has been recorded and can be checked from his publication in 2005.[151] For Si thin film growth and epitaxy, a specific vacuum level and a specific experimental temperature must be achieved so that the Si vapor pressure exceeds that pressure and Si vapor phase for deposition can occur. Furthermore, the vapor pressure of substrate material is required to be lower than that of Si at experimental temperature such that no substrate evaporation is guaranteed.

To summarize, in this chapter we introduce the properties, applications and current researching trend for Si. Si is the second abundant element on our planet which dominates the current semiconductor industries including diodes, transistors, integrated circuits and so on. Also, Si thin films with nano-scale thickness are attracting more and more attentions due to its peculiarity beyond bulk Si such as Dirac-cone-like band structure, QSHE and QAHE, etc.

#### **1.4 Ion Implantation**

Ion implantation is a material synthesis method widely used in semiconductor fabrication and materials research.[54, 143, 152-165] In general, a variety of external species are injected into the target substrate in a very tiny amount to achieve modification of properties or structures. The working mechanism of ion implantation is illustrated in Figure 9 where the whole apparatus consists of three major parts: ion source, accelerator and target.[166] First, a coil made of desired element is heated to enable ionization, ionized elements are excited out of the source and accelerated by the electric field generated within the ion source capacitor. Then, ions traverse the magnetic field to filter impurity ions. Eventually, qualified ions enter the accelerator, further speed up and impinge the substrate. The implanting current is usually set to be small enough to enable accurate content control. Typical ion energies vary from 10 keV to 500 keV: an energy lower than 10 keV results in a narrow penetration of only a few nanometers or less while an energy higher than 500 keV introduces too much damage or even amorphizes the substrate crystals. Doping atoms follow a Gaussian distribution within the substrate. Increasing implantation energy increases the projected range of the dopant atoms. Therefore, it is critical to conduct ion implantation simulations, especially for thin films before actual experiments based on required dopant, dose, target and implanting energy to prevent dopants from penetrating the substrate.

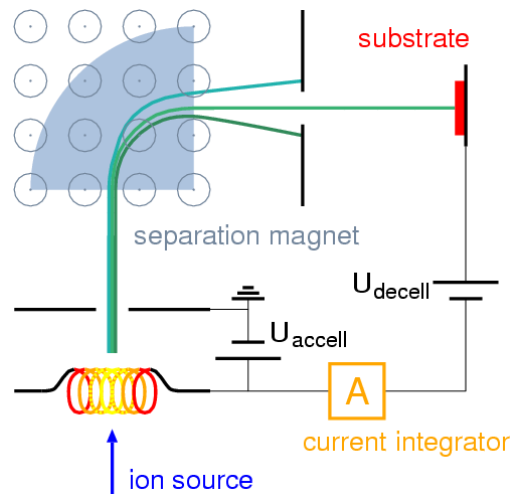


Figure 9. Illustration of ion implantation machine.

Damage introduced by ion implantation is another important factor. First, implanting ions generate point defects within substrate crystals, which is the most common damage introduced by ion implantation. High speed doping ions can either knock target ions off of their original crystal sites thereby leaving vacancies in crystal or substitute target ions by themselves to form interstitial or substitutional defects. Depending on dose (or defect concentration) either vacancies or interstitials change the target crystal structure locally. Furthermore, as-generated point defects are capable of migrating via diffusion and coalescing, giving rise to dislocations loops or other line defects. To recover the doping-induced crystallographic damage, annealing is required after ion implantation to trigger crystal reconstruction.

Second, it is common for target atoms to escape from the surface, known as surface sputtering, resulting from collision between implanting ions and surface atoms. This damage only occurs at large-dose implantation and even leads to surface etching at very large doses. Surface sputtering can be alleviated by subsequent annealing as well. Another typical problem of ion implantation is ion channeling in crystallographic substrates. Ions path along particular crystal directions whose lattices are much more open than others, e.g.  $\langle 110 \rangle$  direction in Si and other diamond-like cubic materials, can be much longer compared to that of other directions, leading to a deeper penetration than those calculated from simulations. In particular, for single crystal substrates, dopants are highly possible to exhibit ion channeling behavior. To avoid ion channeling, ion implantation is usually conducted several degrees off axis.

Ion implantation is of universal application in semiconductor, metal and nano-fabrication. In the semiconductor industry, ion implantation is applied for donor or acceptor doping. Accurate control of doping dose is used to adjust MOSFET threshold

voltages. Ion implantation is also useful in tool steel toughening in which N ions are implanted into tool steel to obtain a strengthened surface capable of resisting crack propagation, fracture and corrosion as interstitial nitrogen inhibits dislocation movement. Ion implantation at high dosage also enables formation of NPs or nanoscale films with the help of particular post processing including thermal annealing, channeling geometry and ion irradiation. In principle, dopants can either remain in solution, react with substrate atoms to generate new chemical species or cluster to form an additional phase, which is controlled by the solute solubility within the target and by the interface energy between dopants and targets. For example, H. Wang et al. synthesize Pb NPs within an epitaxial Al film via ion implantation at the channeling geometry and it is found that the Pb NP size is proportional to the square root of implanting dose, which is interpreted as following diffusion-limited growth kinetics.[54] In this case, Pb atoms assemble into NPs to minimize their surface energy instead of bonding with Al atoms. In contrast, S. Garaj et al. synthesize single layer graphene sheet on Ni(111) single crystal substrate via C ion implantation followed by 1000°C thermal annealing in a high vacuum atmosphere. Upon annealing, C atoms diffuse towards the substrate surface then bond with each other to form a graphene layer, which can be ascribed to the following characteristics of the system: 1) substrate surface with abundant dangling bonds is more energy-favorable for C atoms and 2) small lattice mismatch between Ni(111) facets and graphene makes it a perfect nucleation site for graphene formation and growth.[153] Obviously, a layered structure in this circumstance is more stable than C clusters. Another typical synthesis of layered structure via ion implantation followed by thermal annealing was done by H. S. Tsai et al. in 2016 where they dope B ions into an Al<sub>2</sub>O<sub>3</sub>-capped 4H-SiC wafer to promote the formation of multilayer Si thin films, i.e. silicene.[143] The process is illustrated here in Figure 10 where B ions are implanted at the interface between 180 nm thick Al<sub>2</sub>O<sub>3</sub> thin film and 4H-SiC wafer followed by 1100°C annealing for an hour at N<sub>2</sub>/H<sub>2</sub> atmosphere. Consequently, B ions react with the first several layers of SiC, breaking Si-C bonds and bonding with C themselves, leading to a few layers of bare Si in between. Numbers of silicene layer are primarily controlled by B dose. Al<sub>2</sub>O<sub>3</sub> layer thickness and implanting energy must be pre-calculated to ensure accurate implantation at the interface.

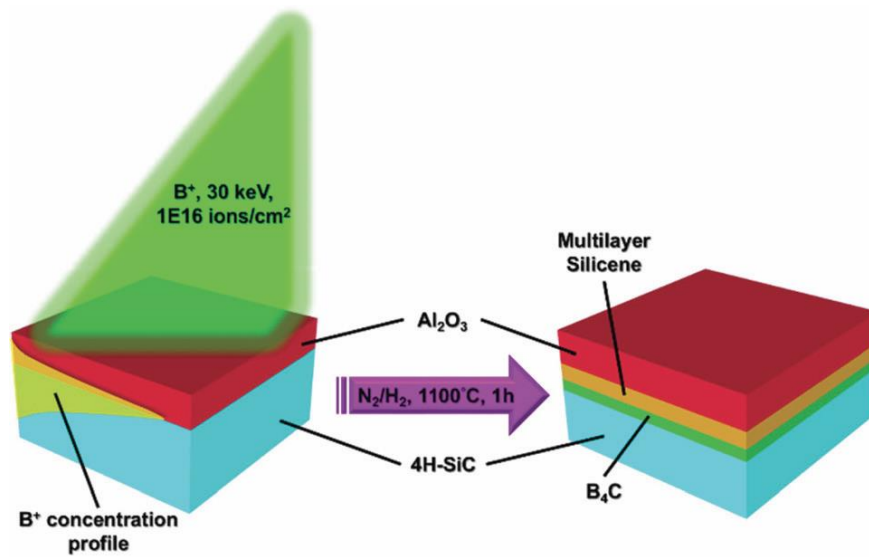


Figure 10. The illustration of the implantation-assisted silicene synthesis process.[143]

To summarize, the mechanism, advantages, weaknesses and conventional applications of ion implantation are introduced in this chapter. It is a doping technique that injects ionized source atoms into target substrates and can be accurately controlled in fluence and distribution. Monte Carlo simulations of ion trajectory into the film can predict their as-implanted distribution. Ion implantation is now widely used in doping, steel toughening and nano-fabrication due to its superiority in process control and is predicted to play a more important role in other material research fields in the future.

### 1.5 Motivations and Aims

As mentioned before Ag is the prior choice for Ohmic contact material due to its excellent electrical and optical performance except for the poor adhesion on substrates. Therefore, we are motivated to develop a novel method to stop Ag thin films from dewetting while maintaining satisfactory electrical and optical performance of Ag films. Our strategy for this purpose is ion implantation due to its capability to administer tiny, highly controlled doses with accurate control. More specifically, we plan to: 1) examine the possible species capable of preventing Ag film from dewetting at a tiny dose while changing the optical and electrical performances of the film as trivially as possible; 2) determine the lowest dose of researched species to stabilize the film morphology, which not only maximize the film quality but also decrease the cost; 3) elucidate the relationship between the film grain size and the implanting dose and establish a suitable grain growth model for Ag thin film in existence of doping species; 4) conduct thermodynamic simulations to analyze Ag dewetting and the influence of external dopants on film wettability; 5) combine the dewetting simulation with grain growth model to predict the dose needed for dewetting prevention at a given temperature; 6)

eventually set up a database to record the wettability change in different dopant-film systems so that any thin film dewetting problems can be solved within a minute.

Moreover, preparing Si thin films with nano-scale thickness is of great importance as well. Thus, we also intend to prepare high quality single crystal Si thin films with a height of a few nanometers via ion implantation followed by thermal annealing. The idea is that 1) implanting Si atoms into Ag film with a pre-calculated dose and 2) annealing the sample at a temperature and vacuum condition to increase the Ag vapor pressure to favor Ag desorption from substrate thereby leaving Si atoms to recrystallize upon the substrate surface. Considering ion implantation enables accurate control of Si doping dose, we are capable of estimating the final Si film thickness via calculation.

In this thesis, we research the effect of external Si and In dopants on Ag thin film dewetting prevention, which helps us master the mechanism of dopant-induced anti-dewetting. We also establish a surface energy model to calculate the critical dose required for dewetting prevention. Furthermore, we research conditions for possible silicene synthesis using ion implantation. Experiments, results, discussion and conclusions are described in the following chapters.

## 2. EXPERIMENTS

### 2.1 Synthesis of Silver Thin Films

2 cm × 1 cm × 0.05 cm single crystal sapphire substrates (AdValue Technology, c-plane, single side polished) were pre-cleaned by dipping into methanol, acetone and SC1 solution (5:1:1 of H<sub>2</sub>O : NH<sub>4</sub>OH : H<sub>2</sub>O<sub>2</sub>) in sequence for 10 min ultrasonic washing, respectively, followed by Ag high-vacuum sputtering (Torr International, Inc.) at room temperature, a base pressure of approximately 5×10<sup>-6</sup> Torr and a working pressure of 1.8×10<sup>-3</sup> Torr. The Ag thin film thickness was controlled to be 100 nm. The working power was ~ 40 W with an Ag deposition rate of ~ 2 Å/s and an Ar flow rate of around 2.3 standard cubic centimeter per minute (sccm). Samples were then stored in a glove box before ion implantation.

### 2.2 Silicon and Indium Implantation

SRIM simulation is done prior to ion implantation in order to ensure that no doping ions penetrated the Ag film into the sapphire substrates directly.[158] 10000 Si or In ions, ionized from a SiH<sub>4</sub> or In<sub>2</sub>O<sub>3</sub> target coil by Ar plasma, respectively, are used for simulation at an implanting energy of 30 keV and the calculated projected range, projected depth and lateral straggling for each species are listed in Table 1. Dopants are expected to follow a Gaussian distribution within the film whose peak concentration, known as projected range, is 17.5 nm and 8.3 nm for Si and In, respectively. The final penetration is calculated to be 61 nm and 29 nm for Si and In, respectively, indicating that 100 nm is thick enough to prevent dopants from reaching the substrate, even if channeling occurs along some Ag grain orientations. The ion distribution curve of Si and In dopants within Ag is shown in Figure 11 in which a) corresponds to Si and b) In.

Table 1. SRIM simulation of Si and In implanting into Ag at 30 keV.

Dopant Species	Projected Range (nm)	Longitudinal Straggling (nm)	Lateral Straggling (nm)	Projected Depth (nm)
Si	17.5	15.2	11.4	61
In	8.3	5.0	3.6	29

Ion implantation is done after SRIM calculation. Ag-capped sapphire substrates are implanted by Si or In ions at an energy of 30 keV and at a UHV of 10<sup>-8</sup> Torr with different implanting doses including 10<sup>14</sup> ions per cm<sup>2</sup>, 10<sup>15</sup> ions per cm<sup>2</sup>, 7×10<sup>15</sup> ions per cm<sup>2</sup>, and 10<sup>16</sup> ions per cm<sup>2</sup>.

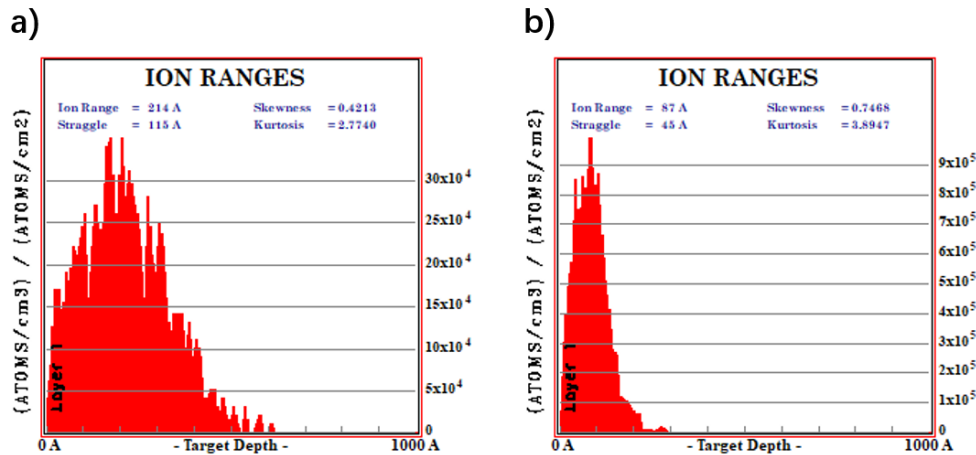


Figure 11. Ion distribution of Si (a) and In (b) dopants with 100 nm thick Ag thin films simulated by SRIM software.

### 2.3 Thermal Annealing and Silver Desorption

After ion implantation two annealing plans are conducted separately in a high vacuum tube furnace under a base pressure of approximately  $10^{-5}$  Torr followed by cold water quenching. First, to observe dewetting features in Ag thin films, implanted samples are annealed at 530°C for different time periods including 0.5 h, 5 h, 10 h, 15 h and 24 h, respectively, enabling us to plot the grain growth diagram. Second, to obtain Si thin films, Ag films after Si implantation are annealed at 900°C for 30 min to enable Ag desorption. Following desorption, the sample is cooled to room temperature inside the furnace.

### 2.4 Characterization and Performance Measurement

Optical microscopy is used to observe macroscale dewetting. Scanning electron microscopy (SEM) (JEOL-7000) is applied to observe changes in Ag film morphology with a beam energy varying from 2 keV to 15 keV. Auger electron spectroscopy (AES) (JEOL JAMP-9500F) is done with an etching depth of 1 nm per step via Ar plasma beam at room temperature. Atomic force microscopy (AFM) (Bruker, Nanoscope\_analysis\_v140r3sr3, contacting mode) is used in ambient conditions to better acquire the grain morphology of the Ag thin film samples. Transmission electron microscopy (TEM) (ThermoFisher FEI Titan 80-300) at 300 keV is used to observe the structure of prepared Si thin films as well as to obtain compositional information using electron energy loss spectroscopy (EELS), Rutherford backscattering spectroscopy (RBS) (Tandem Accelerator, General Ionex) is used to research the Si film concentration and thickness on sapphire substrates.

The average grain size of Ag thin film is calculated via line intercept method proposed by S. A. Butler in 1983, and is simply illustrated here in Figure 12.[167, 168] SEM or AFM images containing more than 50 grains and that exhibiting distinguishable grain boundaries are used for grain size measurement. Equal and paralleled lines are plotted on the image then grain boundaries passing these lines are pointed out, which divides these lines into several unequal sections. Sequentially, the average length of those sections, which can be calculated using the length of the complete line divided by the number of sections, is considered to be the average grain size of the background image. The more paralleled lines we plot within an image, the more accurate our estimated grain size will be.

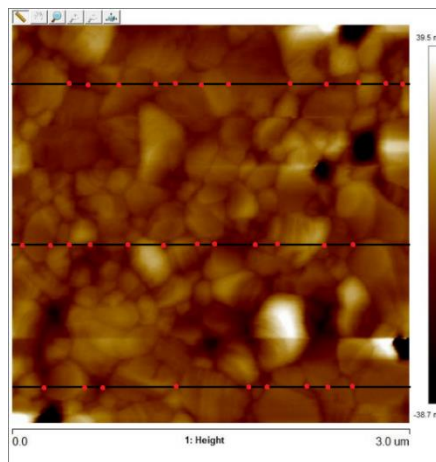


Figure 12. Illustration of line intercept method for grain size calculation.

The film electrical resistivity is measured via the van der Pauw four-point method.[169] As shown in Figure 13, four corners are chosen as contact junctions, two of which connect with a current source while another two with a voltage meter. Then, by rotating the connections four resistances are measured and defined as  $R_1$ ,  $R_2$ ,  $R_3$  and  $R_4$ , corresponding to Figure 13 a-d), respectively. The average resistance of  $R_1$  and  $R_3$  ( $R_{ave, 13}$ ),  $R_2$  and  $R_4$  ( $R_{ave, 24}$ ) are calculated and the higher one of  $R_{ave}$  is defined as  $R_{high}$  while the lower one  $R_{low}$ . Thus, the sample resistivity  $\rho$  is calculated as:

$$\rho = \frac{\pi h}{\ln 2} \cdot \frac{R_{high} + R_{low}}{2} \cdot f\left(\frac{R_{high}}{R_{low}}\right) \quad (4)$$

where  $h$  is the sample height and factor  $f\left(\frac{R_{high}}{R_{low}}\right)$  can be obtained by solving the following equation:

$$\cosh\left[\frac{\frac{R_{high}}{R_{low}} - 1}{\frac{R_{high}}{R_{low}} + 1} \cdot \frac{\ln 2}{f\left(\frac{R_{high}}{R_{low}}\right)}\right] = \frac{1}{2} \exp\left[\frac{\ln 2}{f\left(\frac{R_{high}}{R_{low}}\right)}\right] \quad (5)$$

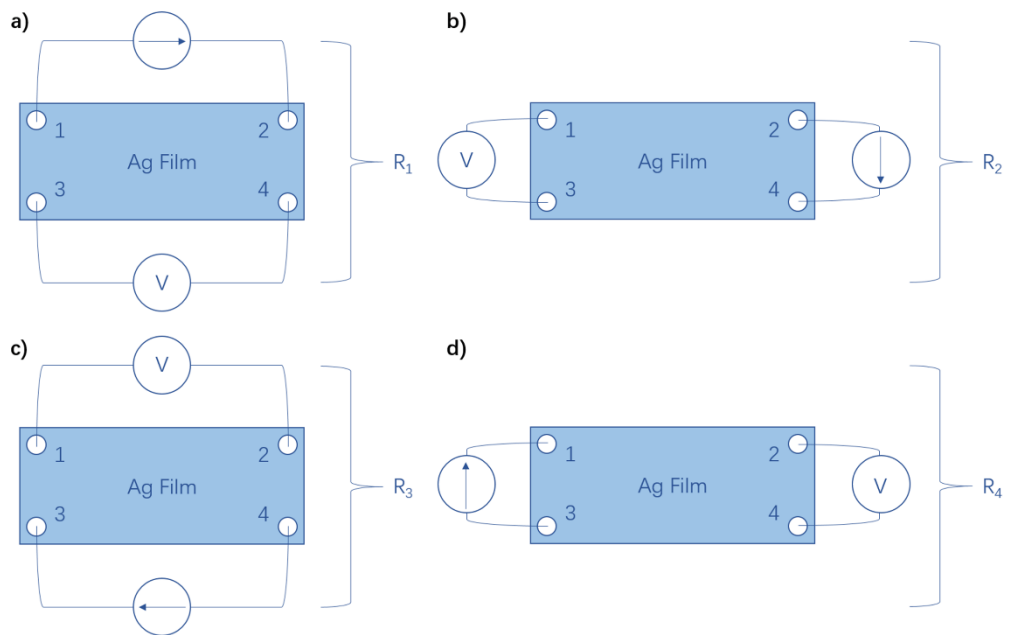


Figure 13. Illustration of van der Pauw four-point method for electrical resistivity measurement.

The film optical reflectivity is measured using spectroscopic ellipsometer (J. A. Woollam Cop.) and is calculated using the EASE software.

### 3. RESULTS AND DISCUSSIONS

#### 3.1 Characterization of Silver Thin Films

Figure 14 shows optical microscopy images of 100 nm thick Ag thin films before and after annealing (530°C, 24 h,  $\sim 10^{-5}$  Torr) where a) and b) correspond to pure Ag and Si-doped Ag thin films, respectively. It is obvious that prior to thermal annealing, both virgin and doped Ag films fully cover the sapphire substrates and no evident distinction can be observed between two films. However, after annealing for 24 h, the virgin Ag film breaks down into small clusters, exposing large patches of the substrate surface, while Si-doped Ag film remains intact and no significant change can be observed from the image.

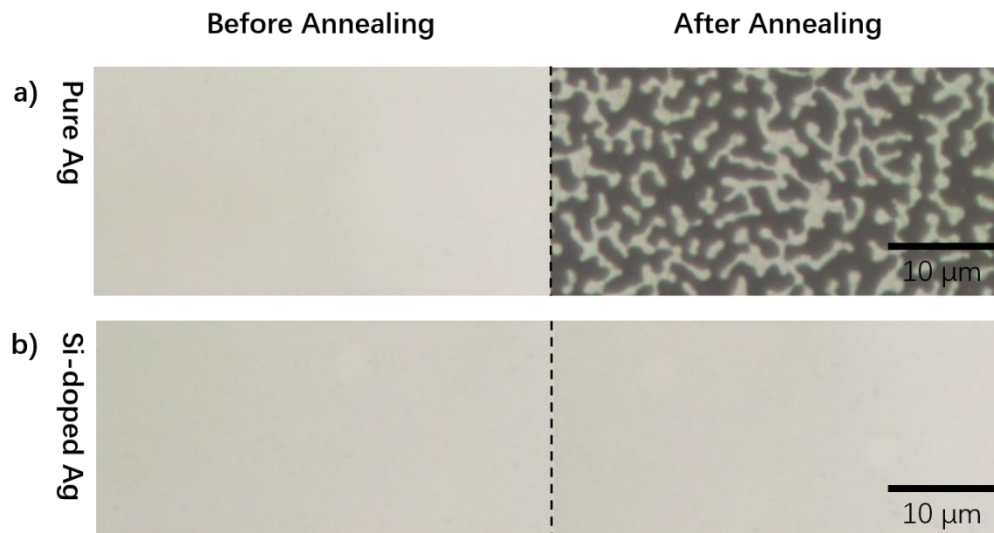


Figure 14. Optical microscopy images of doped and non-doped Ag thin films before and after annealing.

Magnified AFM images for the Ag film are shown in Figure 15 where a-c) represent the pure Ag, Si-doped Ag and In-doped Ag, respectively. Films before annealing are shown on the left while after annealing on the right. Except for changes in film wettability, Ag grains in Si and In doped films after annealing ( $\sim 200$  nm) are much smaller than that in pure Ag films ( $\sim 1000$  nm), indicating that external dopants not only alter the film wettability but also hinder the grain growth. Moreover, it is reasonable to assume that dewetting behavior is strongly related to the film grain growth in that bigger grains are easier to dewet than smaller grains. Such barriers in grain growth contribute to dewetting prevention. This assumption will be confirmed thermodynamically in the following chapters, which also helps us to unveil the mechanism of dopant-induced dewetting prevention.

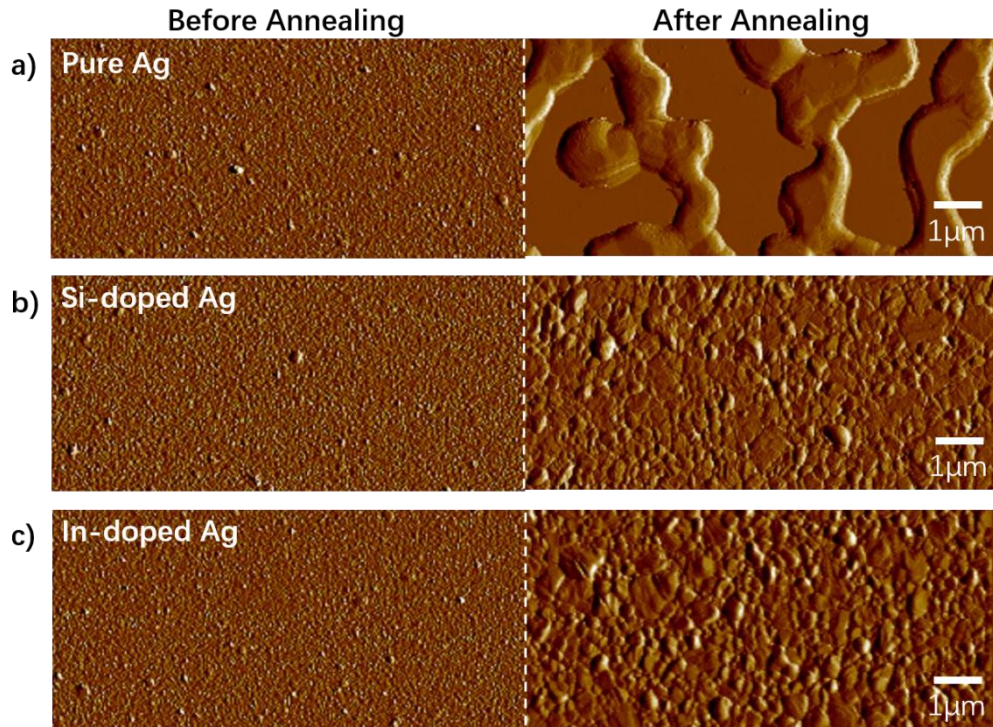


Figure 15. AFM images of pure Ag (a), Si-doped Ag (b) and In-doped Ag (c) thin films before and after annealing.

Si-doped Ag thin films are then researched in particular. Figure 16 exhibits grains in 100 nm thick Ag thin films doped by different amounts of Si with different annealing times, in which a-c) correspond to a Si dose of  $10^{14}$  ions per  $\text{cm}^2$ ,  $10^{15}$  ions per  $\text{cm}^2$  and  $10^{16}$  ions per  $\text{cm}^2$ , respectively; while from top to bottom each line corresponds to an annealing time of 0.5 h, 10 h and 24 h, respectively. Dewetting completely disappears in all three doped samples for more than 24 h and two typical phenomena can be distinguished here: 1) for identical annealing times, the average film grain size decreases gradually with the increasing of doping fluence and 2) even though film grains grow significantly from half-hour to ten-hour annealing times, trivial change is observed from ten-hour to 24 h annealing. The first phenomenon demonstrates our assumption that external doping introduces a retarding force against film grain growth and an increase in dopant concentration retards grain boundary movement. It can be deduced from the second phenomenon that implanting species introduce a size limit during Ag grain growth so that grains fail to expand any more beyond a specific limit (within the time limits of the experiment). As previously mentioned in section 1.2, the dopant-induced grain growth limitation in nanocrystals is known as solute drag and the limiting size can be attributed to the balance of solute concentrations between grains and boundaries. The same solute drag effect also exists in In-doped Ag films, as shown in Figure 17, where dewetting also disappears after 24 h annealing and less-doped Ag

sample contains bigger grains.

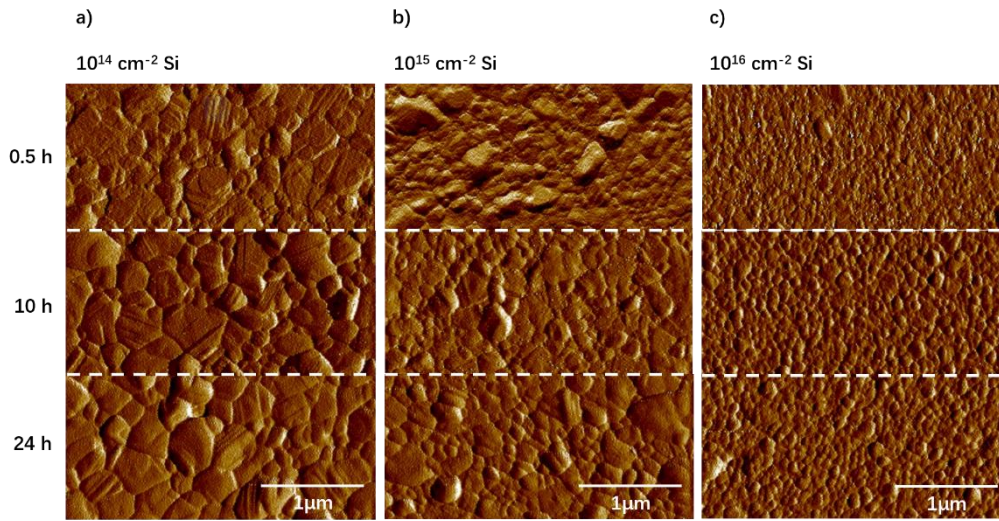


Figure 16. AFM images of Si-doped Ag thin films with different Si dose at different annealing time.

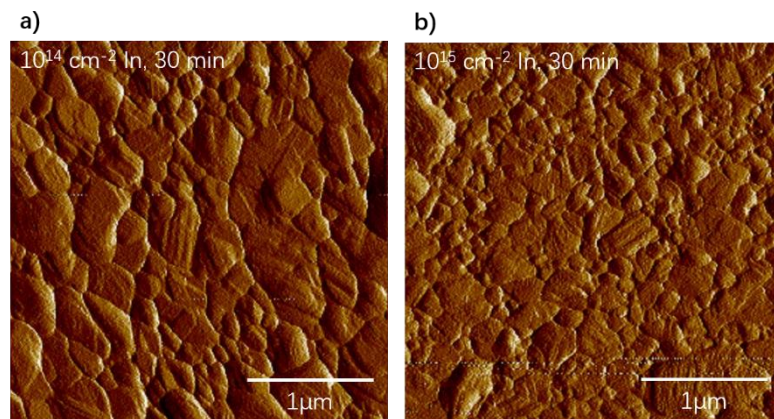


Figure 17. AFM images of In-doped Ag thin films with an In dose of  $10^{14}$  ions per  $\text{cm}^2$  (a) and  $10^{15}$  ions per  $\text{cm}^2$  (b), respectively after a 30 min anneal.

There are two possible paths for Si diffusing within Ag crystals upon annealing: 1) Si atoms attract each other via diffusion to form a continuous phase such as a film or nanoparticles or 2) Si atoms randomly and uniformly distribute within Ag substrate as solute atoms. In order to understand distribution of implanting atoms within the Ag film after isothermal annealing, AES is conducted on the Si-doped Ag samples with a depth profile constructed using Ar ion milling. The depth profile of the Si spectrum is shown in Figure 18 a) and it is clear that a typical Si signal can be found on top of the surface yet the signal decays significantly 2 nm below the surface and disappears completely further away from the top surface. The Si atomic composition along film depth is recorded in Table 2 and is plotted in Figure 18 b), where the Si proportion upon surface turns out to be 4.93% (relative to the top 1 nm planar slab) however decreases to 2.1%

and 0.22% after 1 nm and 2 nm below the surface, respectively, then disappears completely further away from the surface. It can be concluded that 1) Si dopants within the Ag film prefer to diffuse from an original buried Gaussian peak towards the film's top surface upon thermal annealing, as controlled by Fick's law in which atom diffusion follows the concentration gradient. and 2) Si proportion, even the highest 4.93% at top surface, is too low to form a continuous film phase. Thus, implanting Si must exist in Ag as either tiny particles or solute atoms. In comparison with Cahn's Zener drag model, our results are much more similar to Michel's solute drag model in that 1) Ag grains are restricted to a few hundred nanometers and 2) only a tiny amount of Si is implanted. Therefore, we refer to Michel's solute drag model in our research and consider Si as solute atoms within the Ag film.[59]

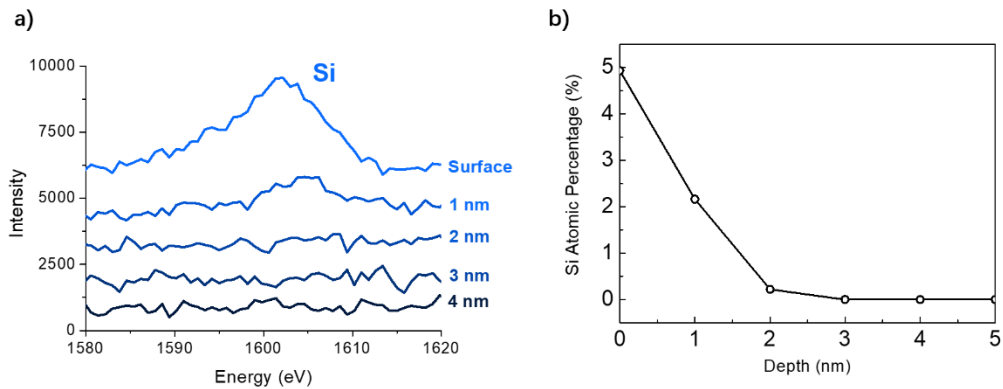


Figure 18. AES spectra for Si-doped Ag thin film where a) is the depth profile of Si spectrum and b) is the calculated Si atomic percentage along depth

Table 2. Si atomic percentage in Ag thin film along depth.

Ag Film Depth (nm)	0	1	2	3	4
Si Atomic Percentage (%)	4.93	2.16	0.22	0	0

To summarize, three typical phenomena are observed by optical microscopy, SEM and AFM: 1) both Si and In doped Ag films remain intact after 24 h isothermal annealing in contrast that pure Ag film breaks down; 2) grain growth in doped Ag thin films is significantly obstructed and an ultimate size is observed during grain growth and 3) the limiting size is dependent on implanting dose in a rule of higher dose corresponding to smaller grains. The AES spectra show that Si dopants prefer to diffuse towards film surface during thermal annealing but may be uniformly distributed within Ag film in the subsurface as solute atoms referring to Michel's solute drag model.

### 3.2 Electrical and Optical Performances of Silicon-Doped Silver Thin Films

In order to determine the influence of external species on the Ag thin film performance,

electrical resistivity and optical reflectivity are measured here for different Si-doped Ag samples and the results are shown in Figure 19. Changes in electrical resistivity, measured via four-point van der Pauw method, as a function of Si dose are recorded in Table 3 and plotted in Figure 19 a). The initial 100 nm thick Ag thin film prior to ion implantation has a resistivity of  $1.59 \times 10^{-8} \Omega \cdot m$ , which is the best conductor used as metallic contact material. Resistivity increases to some extent after Si implantation yet still remains in the same order of magnitude ( $10^{-8} \Omega \cdot m$ ) as that of Cu ( $1.68 \times 10^{-8} \Omega \cdot m$ ) and Au ( $2.44 \times 10^{-8} \Omega \cdot m$ ), suggesting the doped Ag thin film is still an excellent candidate for Ohmic contact applications. Increment in resistivity can be briefly attributed to 1) external species introduce either vacancies or interstitials into Ag crystals thereby significantly decreasing the mean free path of charge carriers and 2) interbonding between Si and Ag atoms alters the films' density of states thus leading to a decrease in carrier concentrations. It is noteworthy that changes in film resistivity as a function of Si dose are not monotonic, suggesting that Si diffusion within Ag film during thermal annealing may be controlled by different mechanisms according to the Si amount.

The optical reflectivity of the Si-doped Ag films also changes trivially according to Figure 19 2d). Ag thin films are widely used as rear contact material in solar cells as a high reflectivity in the visible and near infrared range is required to enable efficient PV structures. The diagram suggests that the reflectivity curves of pure Ag and Si-doped Ag almost coincide with each other. The only outlying curve is from the sample with heaviest-doping. Therefore, we can conclude that the film optical performance also remains the same as long as we maintain a tiny doping dose of Si.

Table 3. Electrical resistivity of Ag thin films doped by different amount of Si.

Si Doping Dose ( $\times 10^{15} \text{ cm}^{-2}$ )	0	0.1	1	7	10
Ag Film Resistivity ( $\times 10^{-8} \Omega \cdot m$ )	1.59	2.76	2.70	2.04	2.43

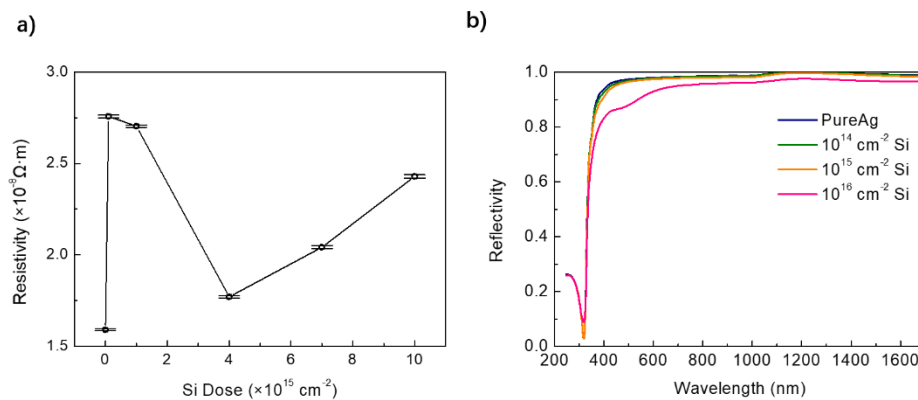


Figure 19. Electrical resistivity (a) and optical reflectivity (b) of Ag thin films varying

in Si implanting fluences.

In total, low-dose implantation trivially affects the electrical and optical properties of Ag thin films. Therefore lightly-doped Ag films are still excellent candidates for Ohmic contacts and plasmonic materials especially after overcoming the dewetting problem.

### 3.3 Silver Grain Growth and Silicon-Induced Solute Drag

#### 3.3.1 Michel's Solute Drag Model for Grain Growth Fitting

As mentioned before grain growth of pure Ag thin films can be expressed by:

$$\frac{dD}{dt} = \frac{\alpha \cdot M_o}{D} \quad (6)$$

where  $t$ ,  $D$  and  $M_o$  represent the annealing time, average Ag grain size at time  $t$  and the grain boundary mobility, respectively.[51-53]  $\alpha$  is an empirical coefficient fitting from experimental data. The function of average grain size with regard to annealing time can then be deduced from equation (6) in an expression of:

$$D(t)^2 - D_o^2 = \alpha \cdot M_o \cdot t \quad (7)$$

where  $D_o$  is the initial average grain size of Ag thin films prior to thermal annealing. Equation (7) describes a parabolic tendency in Ag grain growth, which eventually ends up with infinitely large grains, i.e. single crystal. Unfortunately, the actual grain growth in our 100 nm thick Ag thin films terminates at an average grain size of approximate 1000 nm resulting from the beading of Ag grains. Thus, equation (7) only applies to grain growth of Ag thin film before dewetting and after that Ag grains assemble into isolated islands to terminate planar grain growth.

However, when doped by external Si atoms, Ag grain growth confronts a pinning force, known as solute drag, that significantly decelerates the grain growth rate by that:

$$\frac{dD}{dt} = \frac{\alpha \cdot M}{D} - f \quad (8)$$

where  $M$  is the grain boundary mobility of doped Ag film.  $M$  as a function of solute concentration, referring to Cahn's model, can be expressed by that:

$$M = \frac{1}{\frac{1}{M_o} + \beta \cdot c_{Si}} \quad (9)$$

where  $c_{Si}$  and  $\beta$  represent the Si concentration and an empirical coefficient fitting from experimental data, respectively. The new term  $f$  represents the pinning force, i.e. solute drag. Michel proposes that the pinning force is proportional to both the solute concentration and the grain size:[59]

$$f(c_{Si}, D) = \gamma \cdot c_{Si} \cdot D \quad (10)$$

where  $\gamma$  is the linear coefficient. Then the grain growth rate can be more accurately expressed by substituting equation (9-10) into (8):

$$\frac{dD}{dt} = \frac{\alpha}{\frac{1}{M_o} + \beta \cdot c_{Si}} \cdot \frac{1}{D} - \gamma \cdot c_{Si} \cdot D \quad (11)$$

As is introduced before, inclusion of solute species results in a size limit in grain growth when diffusion of solute species between crystals and boundaries reaches equilibrium. In other words, grain growth rate decreases to zero when reaching the limiting grain size. Therefore, the ultimate grain size  $D_m$  can be derived by setting equation (11) to zero:

$$D_m = \sqrt{\frac{\alpha}{\gamma} \cdot \frac{1}{\left(\frac{1}{M_o} + \beta \cdot c_{Si}\right) \cdot c_{Si}}} \quad (12)$$

In equation (12)  $\alpha$ ,  $\beta$ ,  $\gamma$  and  $M_o$  are temperature-dependent terms only, therefore, during isothermal annealing all those parameters are constant, and the limiting size becomes a unary function with respect to solute concentration. Solving equations 11 and 12, we can derive the average grain size of our Ag thin films as a function of time at a constant temperature and implanting dose:

$$D(t) = \sqrt{D_m^2 - (D_m^2 - D_o^2) \cdot \exp(-2 \cdot \gamma \cdot c_{Si} \cdot t)} \quad (13)$$

Compared to equation (7), the grain growth equation of Si-doped Ag thin films with respect to annealing time follows an exponential tendency instead of parabolic one and in this case a terminal grain size  $D_m$  is introduced to prevent infinite growth of Ag grains. It is necessary to convert dose into concentration in our calculations. The total number of implanting Si atoms equals to the Si dose multiplied by the implanting area. According to Figure 11 dopant concentration follows a Gaussian distribution in the film with a peak concentration at 17.5 nm away from the film surface. For simplification, however, we assume Si dopants are uniformly distributed within the sample therefore the equivalent Si concentration can be calculated using the total number of Si atoms divided by the sample volume:

$$c_{Si} = \frac{D_{Si} \cdot A_{Ag}}{V_{Ag}} \quad (14)$$

where  $D_{Si}$ ,  $A_{Ag}$  and  $V_{Ag}$  represent the Si dose, Ag surface area for ion implantation and Ag sample volume, respectively.

The measured average grain size for each Si dose at different annealing times is recorded in Table 4. It is clear that the measured value changes trivially after 5 h annealing for each dose, demonstrating the existence of limiting grain size. Furthermore, grain growth curve fitting from the measured grain size in Table 4 using equation (12)

and (13) are also plotted in Figure 20. Figure 20 a) describes how the limiting grain size changes with regard to Si fluence where the square, circle, triangle and rhombus symbols correspond to measured average grain size at a Si dose of  $10^{14}$  ions per  $\text{cm}^2$ ,  $10^{15}$  ions per  $\text{cm}^2$ ,  $7 \times 10^{15}$  ions per  $\text{cm}^2$  and  $10^{16}$  ions per  $\text{cm}^2$ , respectively. The decreasing tendency of grain size with the increase in Si dose is evident. The sky blue dashed curve is fitted from equation (12) and it is obvious that the fitting curve deviates substantially from our data points, suggesting the inaccuracy of Michel's solute drag model regarding the Si-Ag system. The average grain size of Ag film as a function of annealing time is also plotted here in Figure 20 b) where, again, the square, circle, triangle and rhombus symbols correspond to measured average grain size at a Si dose of  $10^{14}$  ions per  $\text{cm}^2$ ,  $10^{15}$  ions per  $\text{cm}^2$ ,  $7 \times 10^{15}$  ions per  $\text{cm}^2$  and  $10^{16}$  ions per  $\text{cm}^2$ , respectively. The size limit introduced by doping-induced solute drag becomes more evident in this diagram. Dashed lines here represent the fitting curves obtained using equation (13) and different colors correspond to different Si doses which are consistent with that of symbols. Even though the fitting curve exhibits a size limit in grain growth, the curve severely deviates from our experimental data points, indicating the discrepancies of Michel's solute drag model once relative to our experimental data.

Table 4. Measured average grain size (unit is nm) of Si-doped Ag thin films for different doping fluence at different annealing time.

Si Dose ( $\times 10^{15} \text{ cm}^{-2}$ )	Annealing time (h)					
	0.5	2.5	5	10	17	24
0.1	190.4	232.8	253.5	249.5	253.4	249.0
1	127.6	153.9	159.3	165.0	157.9	156.9
7	81.2	91.7	98.0	94.6	95.1	91.1
10	79.4	91.0	93.8	87.1	90.7	87.2

Table 5. Limiting grain size fitting from our experimental data via equation (10).

$D_m = \sqrt{\frac{\alpha}{\gamma} \cdot \frac{1}{\left(\frac{1}{M_0} + \beta \cdot c_{Si}\right) \cdot c_{Si}}}$	Fitted Limiting Grain Size $D_m$ at Different Si Doping Dose ( $\times 10^{15} \text{ cm}^{-2}$ )			
	0.1	1	7	10
	294.0 nm	93.0 nm	46.5 nm	35.1 nm

In short, Michel's solute drag model satisfies the requirement of size limit during grain growth however fails in match our experimental data points. Therefore, a modified solute drag model is required to better describe the Ag grain growth behavior inclusion of external species.

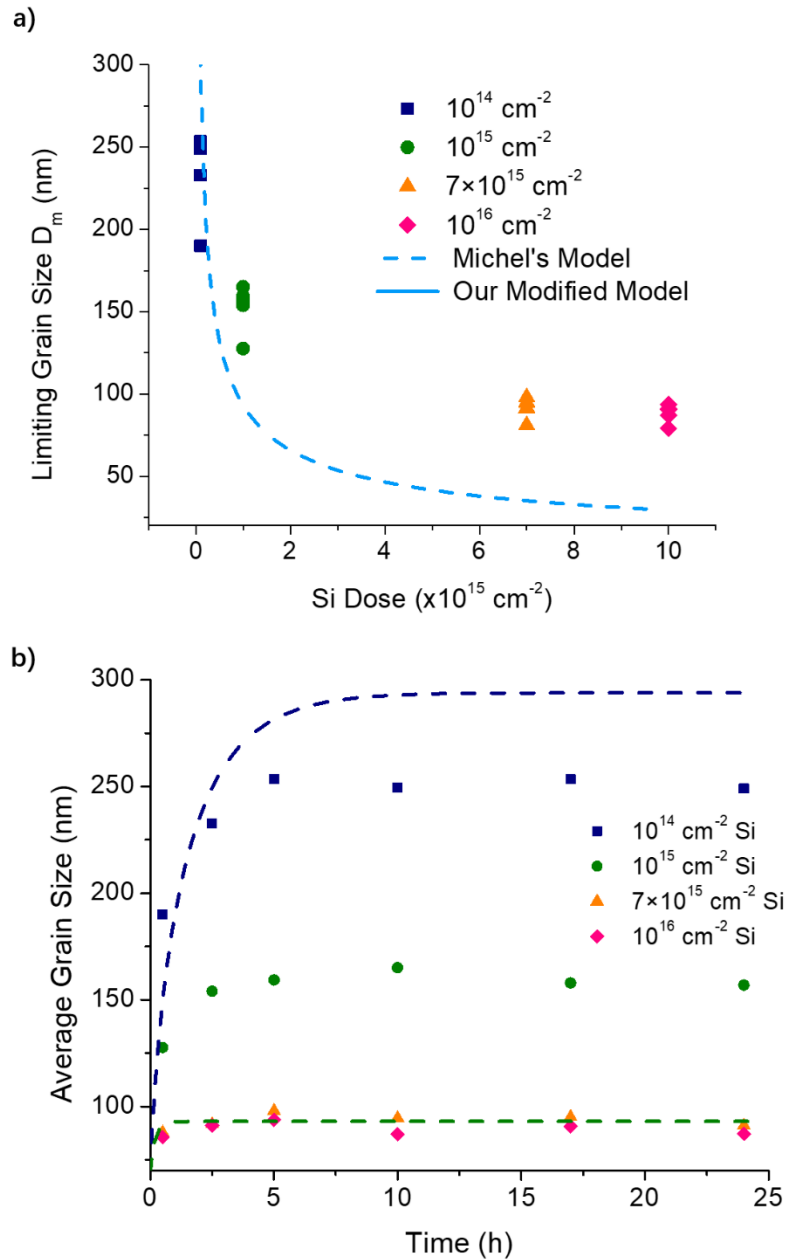


Figure 20. Average grain size of Ag thin films as a function of a) Si implanting dose and b) thermal annealing time based on Michel's solute drag model.

### 3.3.2 Modified Solute Drag Model for Grain Growth Fitting

To better describe the grain growth behavior of our Si-doped Ag thin films, Michel's solute drag model is modified to some extent. The fitting curve in Figure 20 a) drops too quickly to map our data points, suggesting the retarding force introduced by Si dopants is exaggerated especially at high Si doses. In other words, the actual influence of doping content is much gentler than that in Michel's mode. Therefore, we propose

that the retarding force is proportional to the grain size as well as to the solute concentration with a power factor then equation (10) can be rewritten to:

$$f(c_{Si}, D) = \gamma \cdot c_{Si}^m \cdot D \quad (15)$$

where  $m$  is the power index obtained from curve fitting and is temperature dependent only. Substituting equation (15) into equation (9) we obtain:

$$\frac{dD}{dt} = \frac{\alpha}{\frac{1}{M_o} + \beta \cdot c_{Si}} \cdot \frac{1}{D} - \gamma \cdot c_{Si}^m \cdot D \quad (16)$$

Again, setting equation (16) to zero allows us to obtain the expression of limiting grain size  $D_m$ :

$$D_m = \sqrt{\frac{\alpha}{\gamma} \cdot \frac{1}{\left(\frac{1}{M_o} + \beta \cdot c_{Si}\right) \cdot c_{Si}^m}} \quad (17)$$

where  $\alpha$ ,  $\beta$ ,  $\gamma$ ,  $m$  and  $M_o$  are all doping-independent parameters thus at a fixed temperature the grain size limit is merely a function of solute content. Solving equation (16) combined with equation (17) enables us to derive the grain growth function with regard to annealing time:

$$D(t) = \sqrt{D_m^2 - (D_m^2 - D_o^2) \cdot \exp(-2 \cdot \gamma \cdot c_{Si}^m \cdot t)} \quad (18)$$

Curves fitting from equation (17-18) are shown in Figure 21. Figure 21 a) is the average grain size of Ag thin films as a function of Si implanting dose in which the square, circle, triangle, rhombus symbols represent our measured size at a Si dose of  $10^{14}$  ions per  $\text{cm}^2$ ,  $10^{15}$  ions per  $\text{cm}^2$ ,  $7 \times 10^{15}$  ions per  $\text{cm}^2$  and  $10^{16}$  ions per  $\text{cm}^2$ , respectively. The dashed and solid lines correspond to fitting curves based on Michel's model and our modified model, respectively (Michel's model is shown here once more for comparison). As-calculated limiting size for each Si dose is recorded in Table 6 and calculation errors for both Michel's model and our modified model are also listed in Table 7 for comparison. From the diagram we can easily find that the fitting curve of our modified model coincides with the experimental data points perfectly and, accordingly, errors in this fitting curve are less than 5% for all Si doses and no increase tendency in error can be observed from our model. In contrast, errors on the limiting size  $D_m$  calculated from Michel's model reach 17% at the lowest Si dose and amplify substantially with the increasing of Si dose, which further demonstrates the failure of Michel's method in curve fitting and the superiority of our modified model in this circumstance. The power factor  $m$  plays a role in alleviating the retarding effect of solute concentration.  $m$  here is fitted to be 0.41 for our Si-Ag system and a value lower than one is reasonable in decelerating the curve decaying. Unfortunately, we fail to give  $m$  a physical meaning nor can we derive  $m$  from theoretical calculations so until now it is merely a

curve fitting parameter. Intuitively,  $m$  might be related to the diffusion rate of solute species within host crystals considering it alleviates the influence of solute contents during grain growth. It is highly reasonable to assume that a  $m$  reflects the influence of adjacent grain boundaries on bulk concentration of solute species in nanocrystal, which is neglected in Michel's theory. Figure 21 b) is the grain size diagram with regard to annealing time where symbols are experimental data and the square, circle, triangle, rhombus correspond to a Si dose of  $10^{14}$  ions per  $\text{cm}^2$ ,  $10^{15}$  ions per  $\text{cm}^2$ ,  $7 \times 10^{15}$  ions per  $\text{cm}^2$  and  $10^{16}$  ions per  $\text{cm}^2$ , respectively. Solid lines here are grain growth curves fitting from our modified solute drag model and different colors correspond to different Si doses which are consistent with that of symbols. It is evident that curves in Figure 21 b) match closely with our data points, proving a better coherence of our modified model than that of Michel's. Moreover, the grain growth diagram explicitly shows that 1) the existence of limiting grain size for each Si dose and 2) grain growth terminates after 5 h annealing for all samples and more highly-doped sample reaches size limit sooner.

To summarize, grain growth of 100 nm thick Si-doped Ag thin films is researched here, and two conclusions are further confirmed: 1) a size limit for grain growth exists in all Si-doped Ag samples and 2) the limiting size decreases drastically with an increase in solute concentration. Michel's solute drag model first describes such a phenomenon however fails to match our Si-Ag system empirically. Therefore, a modified model is proposed here by introducing a power factor to the solute concentration term in the expression of pinning force. The new model here offers a better match to our experimental data points and less errors in curve fitting, therefore, we will use our modified solute drag model to describe the grain growth behavior of our Si-doped Ag thin films.

Table 6. Limiting grain size fitting from our experimental data via equation (15).

$D_m =$	$m=0.41$			
	Fitted Limiting Grain Size $D_m$ at Different Si Doping Dose ( $\times 10^{15} \text{ cm}^{-2}$ )			
$\sqrt{\frac{\alpha}{\gamma} \cdot \frac{1}{\left(\frac{1}{M_o} + \beta \cdot c_{Si}\right) \cdot c_{Si}^m}}$	0.1	1	7	10
	294.0 nm	93.0 nm	46.5 nm	35.1 nm

Table 7. Error comparison for Michel's model and our modified model in limiting size simulation.

Models and Errors	Si Doping Dose ( $\times 10^{15} \text{ cm}^{-2}$ )			
	0.1	1	7	10
$D_m$ measured from experimental data	251.4 nm	159.8 nm	94.7 nm	89.7 nm

$D_m$ calculated from Michel's model	294.0 nm	93.0 nm	46.5 nm	35.1 nm
$D_m$ calculated from modified model	252.6 nm	155.7 nm	96.0 nm	85.9 nm
Error from Michel's model	17.1%	-41.8%	-50.9%	-60.9%
Error from our modified model	0.5%	-2.5%	1.4%	-4.2%

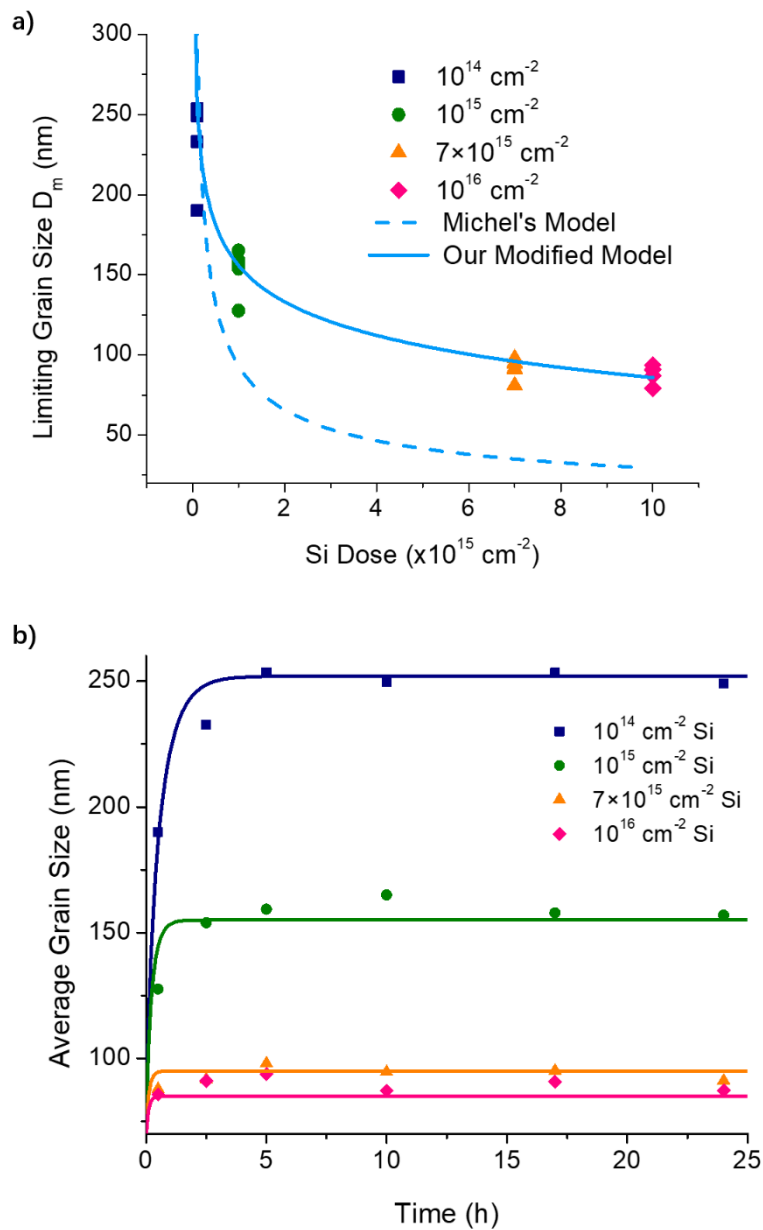


Figure 21. Average grain size of Ag thin films as a function of a) Si implanting dose and b) thermal annealing time based on our modified solute drag model.

### 3.4 Thermodynamic Simulation of Silver Dewetting

#### 3.4.1 Dewetting Mechanism and Hexagonal-Cylinder Grain Model

We have introduced retarded Ag grain growth in existence of solute species in last section and now we will discuss the dewetting mechanism in Ag thin films as well as how dewetting is related to Ag grain growth. Dewetting can be divided into three typical phases, according to the particular grain characteristics in each phase, as shown in Figure 22 in which Figure 22 a) is the continuous film prior to dewetting, defined as phase I, whose grains are relatively small and a top, flat surface. Dewetting initiates at triple grain junctions in the form of tiny pores that can be found at the bottom right corner in Figure 22 a). Figure 22 b) corresponds to a porous film with semi-connecting grains and exposed subsurfaces, defined as phase II. Figure 22 c) exhibits completely beaded grains, defined as phase III, that represents the termination of both grain growth and film dewetting. In general, solid phase dewetting can be described as a time evolutionary process: first, dewetting initiates at triple grain junctions in the form of tiny pores and in the characteristic of grain boundary grooving and surface spherizing (phase I); then, grains and pores enlarge simultaneously, exposing subsurfaces to the air (phase II); eventually, grains separate from each other completely in with characteristically fully spherical surfaces and as isolated islands (phase III).

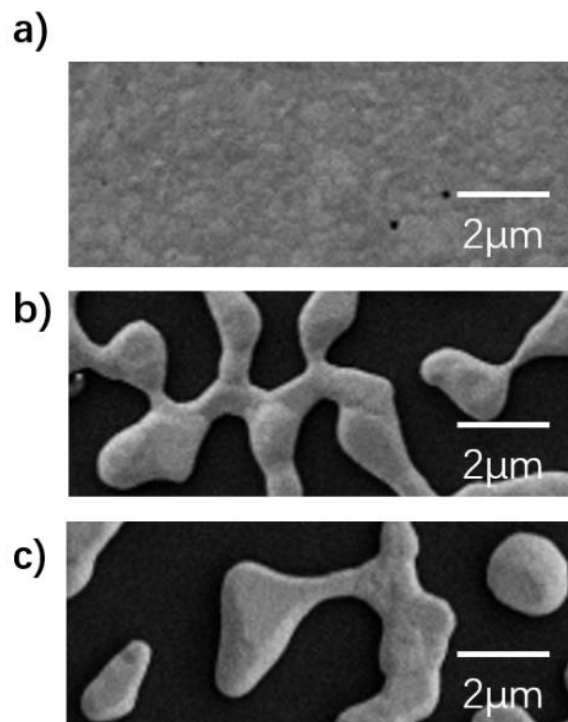


Figure 22. Different phases during dewetting of Ag thin films.

One of the most typical characteristics of thin film dewetting is boundary grooving along with an increase in grain thickness. Figure 23 is an AFM image containing all three dewetting phases in which an increase in grain thickness can be clearly observed. Two white dashed lines are marked in the image that pass through all three phases and their surface profile is shown right beside the image. For the vertical line, the top plane corresponds to phase I where grains are relatively small and thoroughly connected with each other. The height of phase I shown in the depth profile is lowest compared to that of the other two phases, suggesting no surface spherization and boundary grooving in this stage. In the middle part of the vertical line grains are partially connected with each other like peninsulas, which corresponds to phase II. At this stage, film is thicker than phase I but becomes fragmentary. The second- and third-highest peaks in the depth profile, i.e. 414 nm and 358 nm, respectively, all corresponds to phase II and show detachment at the grain boundaries. At the intersection of two dashed lines a fully isolated island is found corresponding to phase III. In this case, grain is fully detached from adjacent grains, possess a spherical grain surface and achieves a maximal grain height, which matches to the highest peak of 477 nm in the surface profile. The lateral dashed line exhibits similar characteristics as its vertical counterpart where the highest 486 nm thick peak corresponds to phase III: discrete islands; another two relatively-low peaks represent phase II: semi-continuous film and the lowest plane is phase I: continuous film.

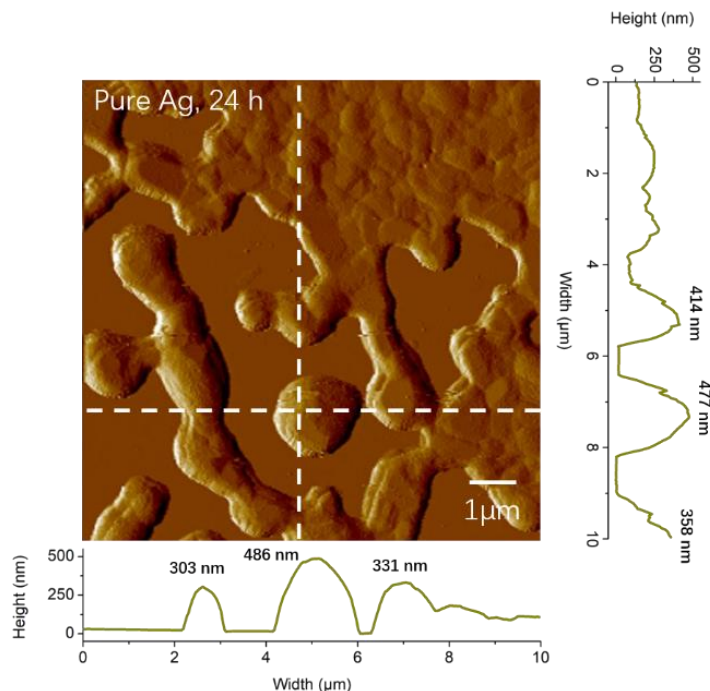


Figure 23. AFM image of a dewetted Ag film which includes all three dewetting phases.

Therefore, a geometric model for dewetting can be established based on the spherizing

characteristic of each phase as discussed above. 2D grains at each phase during dewetting is illustrated in Figure 24. The initial film prior to annealing should be flat and continuous like Figure 24 a); after a short period of annealing film evolves into phase I, as shown in Figure 24 b), where grains still connect each other however grain boundaries groove to some extent and film becomes thicker due to surface spherization. Further annealing generates pores on the film and phase II, porous film, is reached in which grain boundaries further groove and the substrate starts to be exposed to the air, as shown in Figure 24 c). Eventually, film grains fully separate, representing the termination of dewetting; phase III reaches characteristic fully spherical and isolated grains, as shown in Figure 24 d). It is noteworthy that dewetting usually happens along with grain growth thus grains in phase III should be larger than that in phase I and II.

The wetting angle  $\theta$  is used to track the film state at each moment during dewetting and  $\theta$  in each phase is labeled in Figure 24.  $\theta$  keeps changing along with grain boundary grooving until reaching the equilibrium value  $\theta_e$ , therefore, any moment during dewetting corresponds to a specific  $\theta$  value. For example, initial film with flat surface has a wetting angle of  $0^\circ$  and along with dewetting  $\theta$  increases gradually until reaches  $\theta_e$  when there are no more grain boundaries. The critical angles at phase transition points are defined as  $\theta_{crit1}$  and  $\theta_{crit2}$ , corresponding to the transition point at phase I to II and phase II to III, respectively.

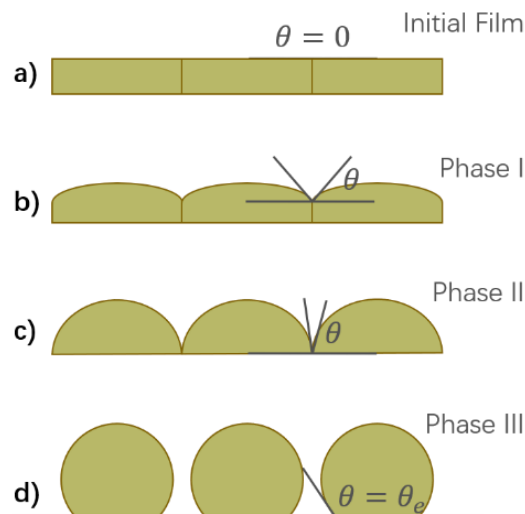


Figure 24. 2D illustration of different phases during thin film dewetting.

Similarly, a 3D grain model for each phase upon dewetting is constructed and shown in Figure 25. This model was first established by K. T. Miller et al. in 1989 to research the dewetting behavior of  $Y_2O_3$  thin films upon thermal annealing.[28] Considering that Ag obeys the same Volmer-Weber mechanism in grain growth as  $Y_2O_3$ , from hereon we refer to the same hexagonal cylinder grain model to describe dewetting of Ag. Miller's

theory assumes that 1) film is thin enough to consist of a single layer of grains only and 2) grains constituting the film are identical and their center position remains constant. Thus, grains in the initial film prior to annealing are considered to be identical hexagonal cylinders with a grain diameter of  $D$  and a film height of  $h$ . The hexagonal shape represents an equilibrium of grain growth because the driving force for boundary motion at triple junction are in balance at an intersection angle of  $120^\circ$ . In other words, Miller's model here ignores the influence of grain size on dewetting but emphasizes changes in grain shape only. Upon dewetting, the initial flat film evolves into uneven film with a curved surface, grooved grain boundaries and an enhanced film thickness, corresponding to phase I. At this stage, the film is still continuous yet its grains reshape to a domed top. Further dewetting generates pores in the film and is defined as phase II in which grains still connect with each other but expose the substrate to the air due to the discontinuity of the vertical boundary facets in phase II. Eventually grain boundaries disappear and the film evolves into discrete islands thoroughly as shown in phase III. In 3D model, each phase can still be distinguished by the wetting angle  $\theta$ , or by the dihedral angle  $\psi$ , and there are two critical angles  $\theta_{crit}$  at phase transition points as well.

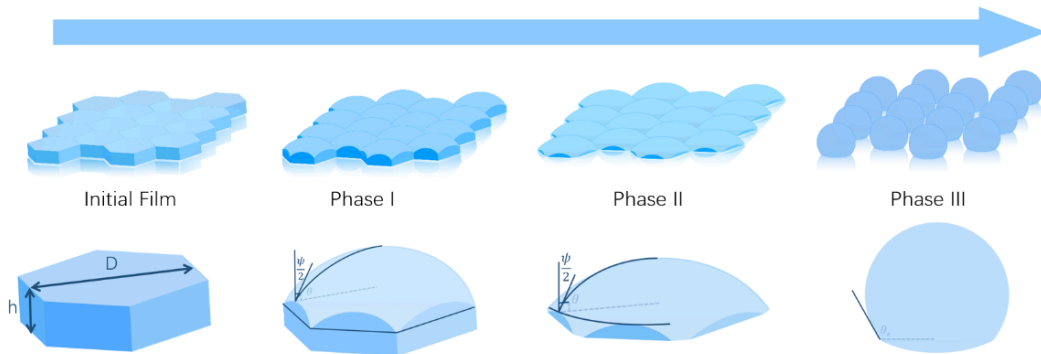


Figure 25. 3D illustration of different phases during thin film dewetting.

In summary, we analyze the dewetting mechanism then set up 3D crystal models to illustrate it in this section. It is believed that dewetting initiates at triple grain junctions as pores inside the film; then film grains and pores enlarge simultaneously, exposing subsurfaces to the air, representing the initial intact film evolving into a porous film. Consequently, dewetting terminates when grain boundaries fully disappear and grain surfaces fully spherize. Three phases are defined here based on different film morphology during dewetting which are phase I: continuous film, phase II: porous film and phase III: discrete islands, respectively. The 3D grain model considers the initial film grains as uniform hexagonal cylinders thus each phase during annealing can be distinguished by varying the wetting angle  $\theta$ .

### 3.4.2 Total Surface Free Energy Calculation

Based on the 3D crystal model constructed in Figure 25, we can calculate the total surface free energy of the Ag thin films in each dewetting phase.[2, 27, 32, 170] First of all, the total surface free energy  $E_{tot}$  is expressed by:

$$E_{tot} = A_s\gamma_s + A_b\gamma_b + A_i\gamma_i + A_{sub}\gamma_{sub} \quad (19)$$

where  $\gamma_s$ ,  $\gamma_b$ ,  $\gamma_i$ ,  $\gamma_{sub}$  represent the grain surface, grain boundary, grain interface and exposed subsurface energy per unit area, respectively, while  $A_s$ ,  $A_b$ ,  $A_i$ ,  $A_{sub}$  correspond to the interface area for each energy, accordingly. Four interfacial energies balance each other in the following expressions as depicted in Figure 26:

$$\gamma_b = 2\gamma_s \cos\left(\frac{\psi_e}{2}\right) \quad (20)$$

$$\gamma_b = 2\gamma_i \cos\left(\frac{\varphi_e}{2}\right) \quad (21)$$

$$\gamma_{sub} = \gamma_s \cos\theta_e + \gamma_i \quad (22)$$

where  $\psi_e$ ,  $\varphi_e$  and  $\theta_e$  corresponds to the grain-air equilibrium dihedral angle, the grain-substrate equilibrium dihedral angle and the equilibrium wetting angle, respectively, and are all labeled in Figure 26 as well.  $\psi_e$ ,  $\varphi_e$  and  $\theta_e$  are set to be  $120^\circ$ ,  $60^\circ$  and  $130^\circ$  for our Ag-Sapphire system, respectively, according to the literature values.[28, 32, 171]  $\theta_e$  is the prior parameter to alter the film wettability, which is calculated from our AFM depth profile in Figure 23 as mentioned before, while  $\psi_e$  and  $\varphi_e$  are set values that trivially influence the film morphology during thermal annealing. Then,  $\gamma_s$ ,  $\gamma_i$  and  $\gamma_{sub}$  can all be expressed by  $\gamma_b$ :

$$\gamma_s = \frac{1}{2}\gamma_b \sec\left(\frac{\psi_e}{2}\right) \quad (23)$$

$$\gamma_i = \frac{1}{2}\gamma_b \sec\left(\frac{\varphi_e}{2}\right) \quad (24)$$

$$\gamma_{sub} = \frac{1}{2}\gamma_b \cdot \left(\sec\left(\frac{\psi_e}{2}\right) \cdot \cos\theta_e + \sec\left(\frac{\varphi_e}{2}\right)\right) \quad (25)$$

By the way, dihedral angle  $\psi$  and wetting angle  $\theta$  are related by equation (26):

$$\Psi = 180^\circ - 2\theta \quad (26)$$

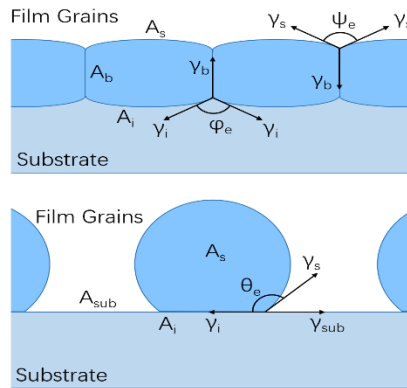


Figure 26. Illustration of interface energy in equilibrium.

Four interface areas at each phase can be calculated based on our hexagonal cylinder grain model then the total surface free energy is obtained from equation (19). Flat grains in initial film prior to thermal annealing is shown in Figure 27 in which grains are considered to be identical hexagonal cylinders with an average grain diameter  $D$  and grain height  $h$ . Four interface areas are calculated by equations listed in Table 8. The total surface free energy of initial film is defined as initial energy  $E_i$ , and is used as a normalization factor.

Table 8. Interface area of grains in initial film.

Interface Area	Formula
$A_s$	$D^2 \frac{\sqrt{3}}{2}$
$A_b$	$D^2 \frac{\sqrt{3}}{D/h}$
$A_i$	$D^2 \frac{\sqrt{3}}{2}$
$A_{sub}$	0

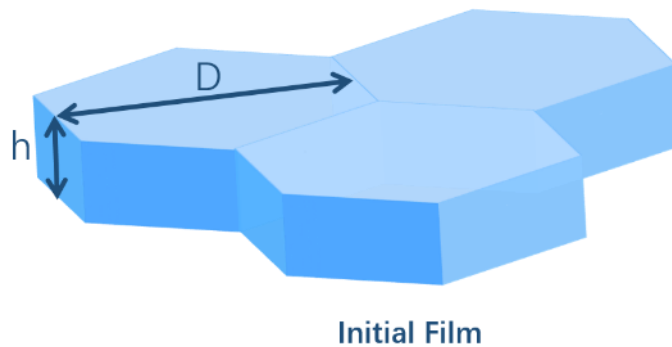


Figure 27. Illustration of grain in initial film.

Grains in phase I are shown in Figure 28 and essential parameters are labeled in the figure. The film at this stage is still continuous yet displays grooves at grain boundaries. Calculated interface areas of phase I are listed in Table 9.

Table 9. Interface area of grains in phase I.

Surface Area	Formula
$A_s$	$\frac{D^2}{4\sin^2\theta} \left( \frac{A_{cap} - 6A_{wedge}}{a^2} \right)$
$A_b$	$3D^2 \left[ \frac{f_p}{\sqrt{3}\frac{D}{h}} + \left( \frac{1}{4\tan^2\theta} \right) \sin^{-1} \left( \frac{\tan\theta}{\sqrt{3}} \right) - \frac{\sin\gamma}{4\sqrt{3}\sin\theta} \right]$
$A_i$	$D^2 \frac{\sqrt{3}}{2}$
$A_{sub}$	0

where  $a$ ,  $A_{cap}$  and  $A_{wedge}$  are the spherical cap radius, spherical cap area and wedge area, respectively, and can be derived by:

$$A_{cap} = 2\pi a^2(1 - \sin\gamma) \quad (27)$$

$$A_{wedge} = 2a^2 \left[ -\alpha\sin\gamma + \int_0^\alpha \left( 1 - \frac{\cos^2\gamma \cos^2\alpha}{\cos^2\theta} \right)^{\frac{1}{2}} d\theta \right] \quad (28)$$

where  $\theta$  is the wetting angle and the wedge angle  $\alpha=30^\circ$  for phase I.  $\gamma$  can be related to  $\theta$  by the equation:

$$\cos\gamma = \frac{2\sin\theta}{\sqrt{3}} \quad (29)$$

$f_p$  is the pillar height fraction and can be expressed by:

$$f_p = 1 - \frac{D}{h} \cdot \frac{(V_{cap} - 6V_{wedge})}{4\sqrt{3}a^3\sin^3\theta} \quad (30)$$

where  $V_{cap}$  and  $V_{wedge}$  are spherical cap volume and wedge volume, respectively, and can be derived by:

$$V_{cap} = \frac{\pi}{3} a^3(2 - \sin\gamma + \sin^3\gamma) \quad (31)$$

$$V_{wedge} = a^3 \left[ \sin\gamma \left( \frac{\alpha \sin^2\gamma}{3} - \alpha + \cos^2\gamma \sin\alpha \cos\alpha \right) + \frac{2}{3} \int_0^\alpha \left( 1 - \frac{\cos^2\gamma \cos^2\alpha}{\cos^2\theta} \right)^{\frac{3}{2}} d\theta \right] \quad (32)$$

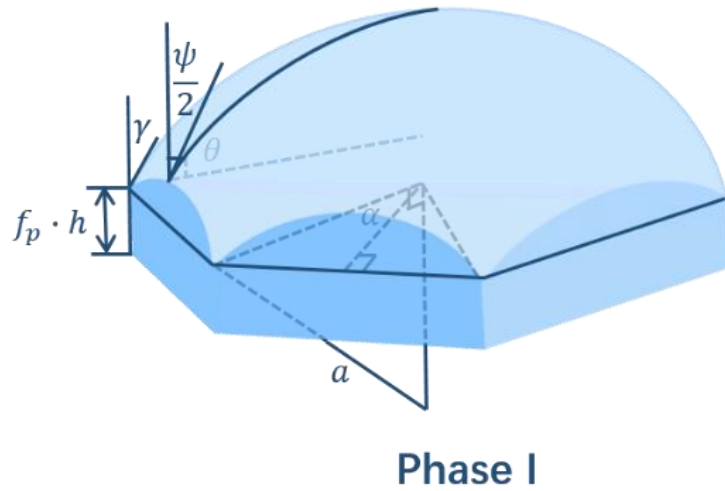


Figure 28. Illustration of grain in phase I: continuous film.

Grains in phase II are shown in Figure 29 and essential parameters are labeled in the figure as well. Grooving further develops and poles appear in this stage and film evolves into a semi-continuous morphology. Calculated interface areas at phase II are listed in Table 10.

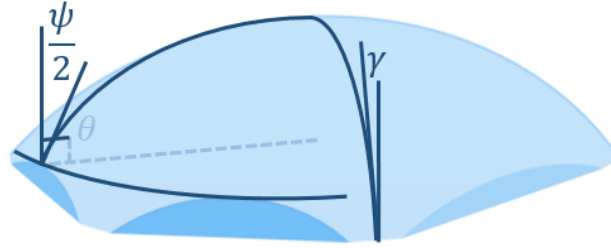
Table 10. Interface area of grains in phase II.

Surface Area	Formula
$A_s$	$\frac{D^2}{4\sin^2\theta} \left( \frac{A_{cap} - 6A_{wedge}}{a^2} \right)$
$A_b$	$\frac{3D^2}{4\sin^2\theta} \left[ \cos^2\theta \tan^{-1} \left( \frac{\cos\gamma \sin\alpha}{\sin\gamma} \right) + \cos\gamma \sin\gamma \sin\alpha \right]$
$A_i$	$\frac{3D^2}{2} \left( \tan\alpha + \frac{\frac{\pi}{6} - \alpha}{\cos^2\alpha} \right)$
$A_{sub}$	$\frac{D^2}{2} \left[ \sqrt{3} - 3 \left( \tan\alpha + \frac{\frac{\pi}{6} - \alpha}{\cos^2\alpha} \right) \right]$

$\alpha$ , in this case, varies from  $30^\circ$  to  $0$  and can be determined by:

$$\cos\gamma = \frac{\sin\theta}{\cos\alpha} \quad (33)$$

$$\frac{D}{h} = \frac{4\sqrt{3}a^3 \sin^3\theta}{V_{cap} - 6V_{wedge}} \quad (34)$$



**Phase II**

Figure 29. Illustration of grain in phase II: porous film.

Grains separate from each other suggesting phase III is reached in the mean while dewetting and grain growth terminate. Illustration of phase III is shown in Figure 30 as well as critical parameters required for interface calculation. Interface areas for this phase are listed in Table 11.

Table 11. Interface area of grains in phase III.

Surface Area	Formula
$A_s$	$D^2 \left[ \frac{2\pi(1 - \cos\theta)}{\sin^2\theta} \right] R_c^2$
$A_b$	0
$A_i$	$D^2 \pi R_c^2$
$A_{sub}$	$D^2 \left( \frac{\sqrt{3}}{2} - \pi R_c^2 \right)$

where the radius of the spherical cap  $R_c$ , normalized by the initial grain diameter  $D$ , can be expressed by that:

$$R_c = \frac{\sqrt{3}\sin\theta}{\left[ 2\pi \frac{D}{h} (2 - 3\cos\theta + \cos^3\theta) \right]^{\frac{1}{3}}} \quad (35)$$

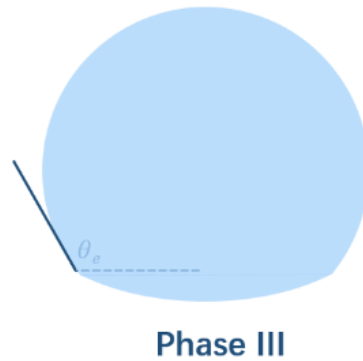


Figure 30. Illustration of grain in phase III: discrete islands.

It is noteworthy that two critical wetting angles can then be derived:  $\theta_{crit1}$  is obtained when the pillar height fraction  $f_p$  equals to zero, i.e. setting equation (30) to zero, and  $\theta_{crit2}$  is obtained by solving equation (33-34) when the wedge angle  $\alpha$  equals to zero.

Hereby, we have summarized all equations required for thermodynamic simulation of thin film dewetting at each phase thus we are now capable of calculating the total surface free energy of our Ag thin films.

### 3.4.3 Dewetting Simulation along with Grain Growth

Substituting the interface areas in Table 7-10 into equation (19) enables us to obtain the total surface free energy  $E_{tot}$  normalized by the initial energy  $E_i$  as a function of the wetting angle  $\theta$  and the grain diameter-to-height ratio  $\frac{D}{h}$ :

$$\frac{E_{tot}}{E_i} = f\left(\theta, \frac{D}{h}\right)_{\psi_e, \varphi_e, \theta_e} \quad (36)$$

Regardless of dewetting and surface spherizing, grain boundaries only migrate in-plane during grain growth so that the grain height  $h$  remains constant while the grain diameter  $D$  increases gradually upon thermal annealing. AFM image in Figure 31 clearly shows the thickness of our Ag thin film to be  $h = 100$  nm. The average grain size  $D$  varies upon thermal dewetting and has been recorded here in Table 4. Thus, the total surface energy normalized by initial energy  $\frac{E_{tot}}{E_i}$  as a function of wetting angle  $\theta$  can then be calculated and plotted, enabling us to determine the equilibrium state at a known  $\frac{D}{h}$  value.

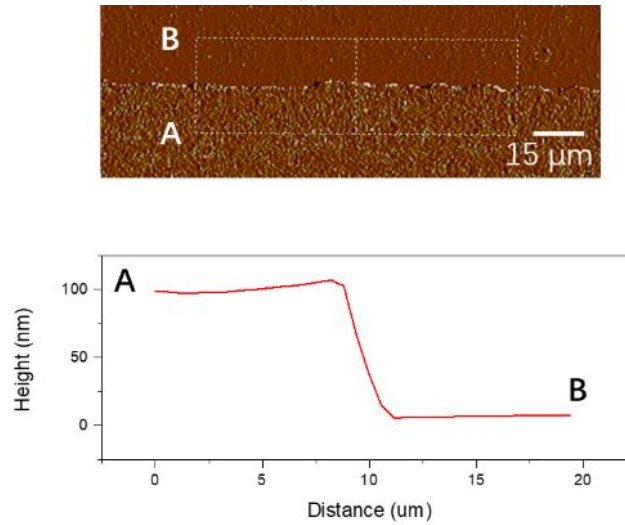


Figure 31. AFM images of the edge of our Ag thin film.

Figure 32 exhibits the normalized energy  $\frac{E_{tot}}{E_i}$  of our pure Ag thin film as a function of wetting angle  $\theta$  before (navy blue dashed line) and after 24 h isothermal annealing (sky blue dashed line). Before annealing, the average grain size of Ag thin film is calculated to be 70 nm then dividing by the film thickness of 100 nm we obtain a diameter-to-height ratio of  $\frac{D}{h}|_{t=0} = 0.7$ ; while after 24 h annealing the average grain size of ruptured Ag film increases to  $\sim 1000$  nm thus the diameter-to-height ratio now changes to  $\frac{D}{h}|_{t=24 h} = 10$ . It is clear that before annealing, the most stable state corresponds to the wetting angle of  $30^\circ$ , or the equilibrium dihedral angle  $\psi_e = 120^\circ$ , at phase I, which means the most stable state for initial film is phase I: continuous film. However, after 24 h annealing, the most stable state transfers to  $\theta = \theta_e = 130^\circ$ , indicating the equilibrium state is reached and the film stabilizes in phase III: discrete islands. In short, the minimum-energy state of the Ag film transfers from phase I before annealing to phase III after annealing, indicating the most stable state of the film also transfers from continuous film before annealing to isolated islands after annealing. Only phase I shows up in the normalized energy curve before annealing, suggesting the normalized energy in phase II and III is higher than one thus being screened here. Energy curve after 24 h annealing shows three phases evidently and two critical wetting angles, i.e.  $\theta_{crit1}$  and  $\theta_{crit2}$ , at phase transition points are marked in the diagram. Phase I corresponds to a wetting angle range between  $0^\circ$  and  $30^\circ$  while phase II matches to a range between  $30^\circ$  and  $45^\circ$  and wetting angle higher than  $45^\circ$  belongs to phase III. It is meaningless to compare the normalized energy value at different annealing times because the normalized energy is a relative value and the absolute value of total free

surface energy is not derived here. Therefore, the primary function of our energy distribution curve is to find the equilibrium phase during dewetting based on the wetting angle at equilibrium state, i.e. minimum energy state.

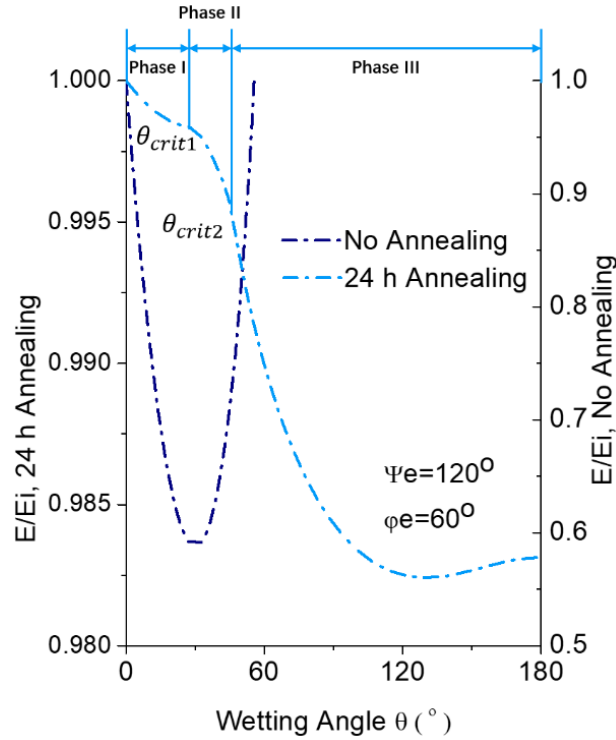


Figure 32. Normalized energy distribution as a function of wetting angle  $\theta$  of pure Ag film before and after annealing.

We have already discussed the influence of Si implanting dose on Ag grain size and now we will figure out how the doping dose affects the Ag grain energy distribution.

The normalized grain energy  $\frac{E_{tot}}{E_i}$  as a function of wetting angle  $\theta$  of the 100 nm thick

Ag thin film implanted by different doses of Si after 24 h annealing is plotted in Figure 33 where the sky blue, navy blue, green, orange and pink circles correspond to a Si dose of  $10^{14}$  ions per  $\text{cm}^2$ ,  $10^{15}$  ions per  $\text{cm}^2$ ,  $7 \times 10^{15}$  ions per  $\text{cm}^2$  and  $10^{16}$  ions per  $\text{cm}^2$ , respectively. Again, we should emphasize on the changes in wetting angle at the minimum-energy state instead of the normalized energy value. We demonstrated in section 3.3 that higher implanting dose obtained smaller limiting grain size, which means smaller diameter-to-height ratio  $\frac{D}{h}$  at a constant film thickness  $h$ . The diagram

shows that after doping the minimum-energy state transfers from phase III at  $\theta=130^\circ$  to phase I at  $\theta=30^\circ$ , indicating the doped film remains continuous after annealing rather than rupture into particles as the pure Ag film did. The simulation of stable phase is consistent with our experimental results. It is of great interest that Ag films, whatever

the Si dose, stabilize at the equilibrium dihedral angle of  $\psi_e=120^\circ$ , i.e.  $\theta=30^\circ$ , supporting that the most stable state for phase I must corresponds to a same equilibrium state of  $\theta=30^\circ$ .

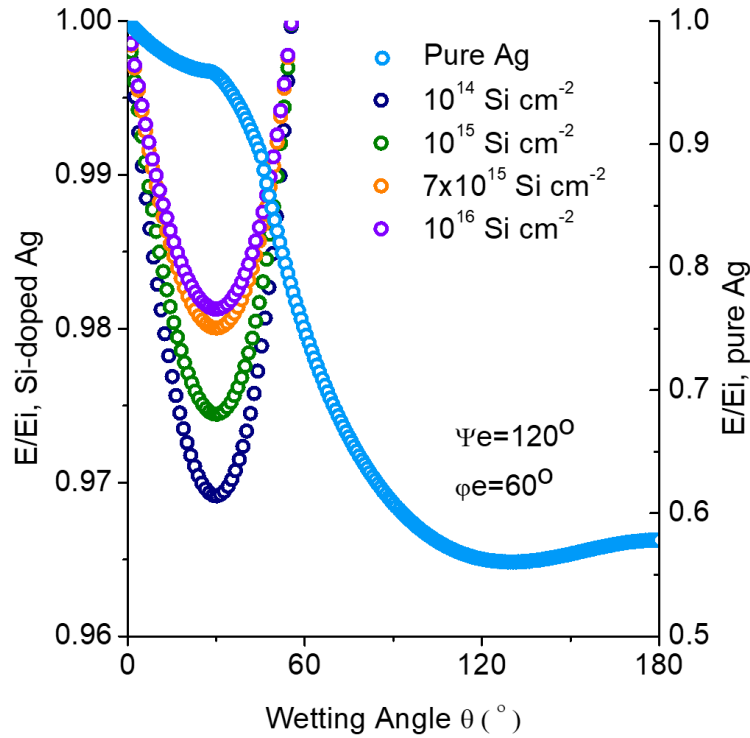


Figure 33. Energy distribution of Ag thin films doped by different dose of Si after 24 h thermal annealing.

This theory can expand to different film-substrate systems by plotting a phase diagram with regard to the grain diameter-to-height ratio  $\frac{D}{h}$  and to the equilibrium wetting angle  $\theta_e$ . The phase diagram enables us to determine the equilibrium phase at a given  $\frac{D}{h}$  and  $\theta_e$ , which is obtained by calculating the wetting angle  $\theta$  of the minimum-energy state at the required  $\frac{D}{h}$  and  $\theta_e$  and then matching  $\theta$  with its stable phase. The diagram is plotted in Figure 34 where each phase stabilizes in a specific region. The bottom part is the stable region for phase I with relatively small diameter-to-height ratio  $\frac{D}{h}$ . It is noteworthy that the critical wetting angle  $\theta_{crit2}$  at the transition point between phase II and III cannot exceed  $180^\circ$ , accordingly,  $\frac{D}{h}$  is calculated to be no less than  $6\sqrt{3}/\pi$  for phase III. The stable region for phase II locates in the top left part of the diagram with low  $\theta_e$  and large  $\frac{D}{h}$ , while the broad region at top right corner of the phase

diagram matches to the stable region of phase III. The diagram clearly shows that to prevent thin film dewetting small  $\frac{D}{h}$  is required, which can be achieved either by decreasing the average grain size  $D$ , like our strategy of employing solute drag effects, or by increasing the film thickness  $h$ . As mentioned before, equilibrium wetting angle  $\theta_e$  of our Ag-sapphire system is  $130^\circ$  thus any state of Ag must sit on the vertical line at  $\theta_e=130^\circ$ . The light blue and sky blue circles represent the pure Ag film before and after annealing, respectively. As mentioned before,  $\frac{D}{h}$  changes from 0.7 before annealing to 10 after annealing, therefore, the equilibrium state of the film also transfers from phase I, continuous film, to phase III, isolated islands, according to the phase diagram. Navy blue, green, orange and pink circles represent the annealed Ag film doped by  $10^{14}$  Si per  $\text{cm}^2$ ,  $10^{15}$  Si per  $\text{cm}^2$ ,  $7 \times 10^{15}$  Si per  $\text{cm}^2$  and  $10^{16}$  Si per  $\text{cm}^2$ , respectively. It is evident that inclusion of external species enables their free energies to remain in phase I rather than phase III due to solute drag, thus Si-doped films remain intact even after annealing.

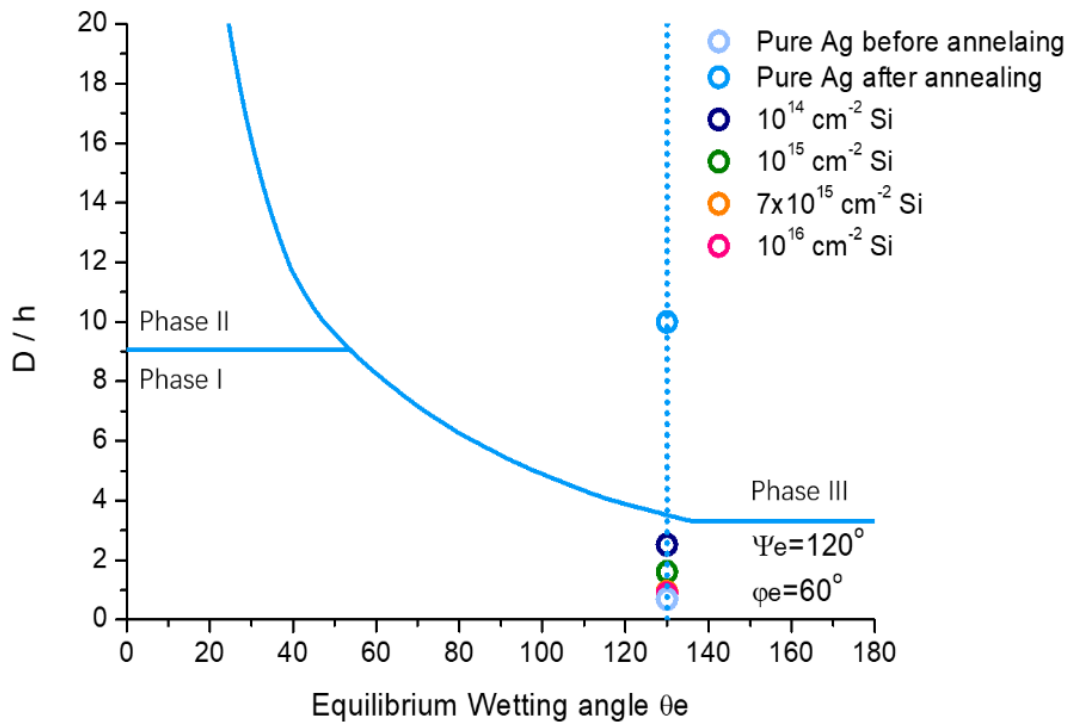


Figure 34. Phase diagram of film-substrate system.

It is noteworthy that blue lines in the phase diagram represent the threshold between phase transformation and for Ag whose  $\theta_e=130^\circ$   $\frac{D}{h}$  upon the border is calculated to be 3.5 in between phase I: continuous film and III: beaded islands. Therefore, the critical

grain size for a 100 nm thick Ag thin film is 350 nm above which film aggregates after annealing. As introduced before, the limiting grain size of Ag films can be controlled by the implanting dose of external Si as summarized in equation (17). Therefore, we are capable of calculating the critical Si dose at which Ag grains reach the critical limiting size, i.e. 350 nm. The limiting grain size as a function of Si dose is again plotted in Figure 35 (blue solid line) while the critical size to initiate dewetting is labeled by the gray dashed line. Two curves intersect at a Si dose of  $2.0 \times 10^{13}$  ions per  $\text{cm}^2$  that is the lowest dose required to prevent 100 nm thick Ag thin film from dewetting. Unfortunately, control of doping at this level is difficult to achieve in 100 nm films. Further experiments will be undertaken to formulate a test of this prediction.

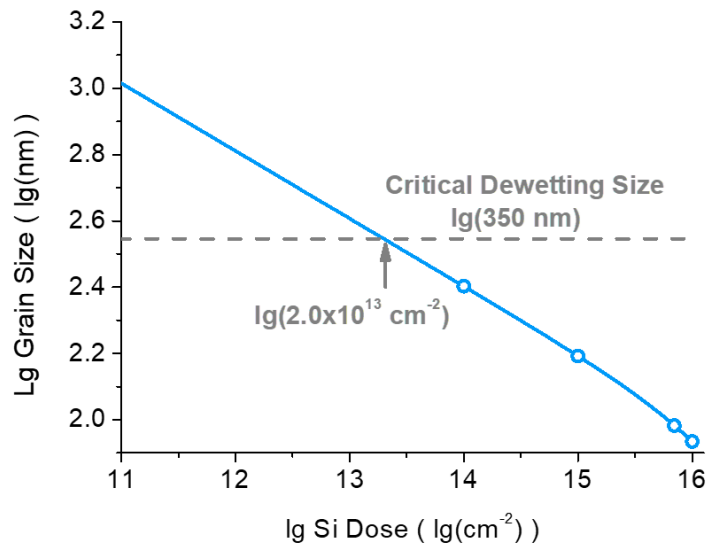


Figure 35. Critical dewetting size in the limiting grain size curve calculated from our modified solute drag model.

To summarize, in this section we introduce a thermodynamic model to simulate the total surface free energy distribution of Ag grains during Ag film dewetting. It is found that after annealing grains in pure Ag films minimize their total surface free energy in phase III: isolated islands while Si-doped Ag films in phase I: continuous film, suggesting the equilibrium state for Ag film switches from aggregated beads to continuous film due to external doping. Combining our modified solute drag model with the thermodynamic simulation we predict the critical grain diameter to initiate agglomeration of 100 nm thick Ag thin film is 350 nm and the critical Si dose to prevent 100 nm thick Ag thin film from dewetting is  $2.0 \times 10^{13}$  ions per  $\text{cm}^2$ .

### 3.5 Silicon Thin Film Synthesis via Ion Implantation

Si thin films are also obtained from our Si-doped Ag films by higher temperature

annealing. The idea originates from Slaven's research on graphene in 2010 where they implanted carbon atoms into a Ni(111) film followed by thermal annealing so that as-implanted C atoms diffused towards the Ni surface during annealing and reconstructed to a single layer, i.e. graphene.[153] Similarly, we try to synthesize monolayer silicon, designated as silicene, using the same implantation-plus-annealing strategy. What makes our research unique is that, compared to carbon who is thermodynamically favorable to diffuse upon the surface, diffusion of Si within Ag(111) film is unpredictable. Thus we decided to desorb Ag film directly to ensure all Si atoms precipitate down to the substrate surface by reasoning that Si has a lower vapor pressure than Ag. For this purpose, 100 nm thick Ag thin films doped by  $10^{16}$  Si per  $\text{cm}^{-2}$  (8 Si monolayers) are annealed at  $900^\circ\text{C}$  with a pressure of  $10^{-6}$  Torr for 30 min to enable Ag desorption from the sapphire substrate. Furthermore, as-synthesized Si films can be patterned if is performed through a mask prior to desorption. Experiment is illustrated in Figure 36 where a TEM sample grid is used as mask during ion implantation and after  $900^\circ\text{C}$  annealing for 30 min. Ag disappears and Si left with a grid pattern. Vapor pressure of Ag and Si is shown in Figure 37 and we can tell from the diagram that at  $900^\circ\text{C}$  the vapor pressure of Si ( $10^{-8}$  Torr) is much lower than that of Ag ( $10^{-3}$  Torr), indicating that in our circumstance with a temperature of  $900^\circ\text{C}$  and a pressure of  $10^{-6}$  Torr Ag will definitely evaporate while Si remains in a solid phase.[172]

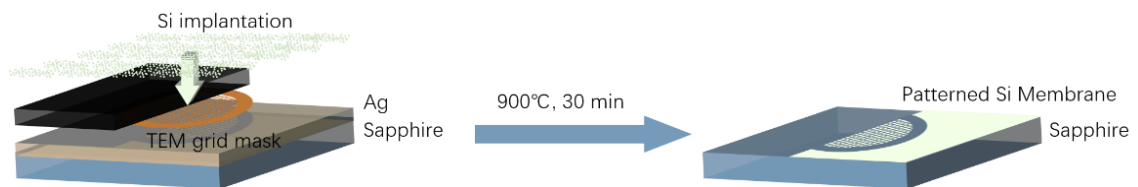


Figure 36. Illustration of patterned Si thin film synthesis by ion implantation.

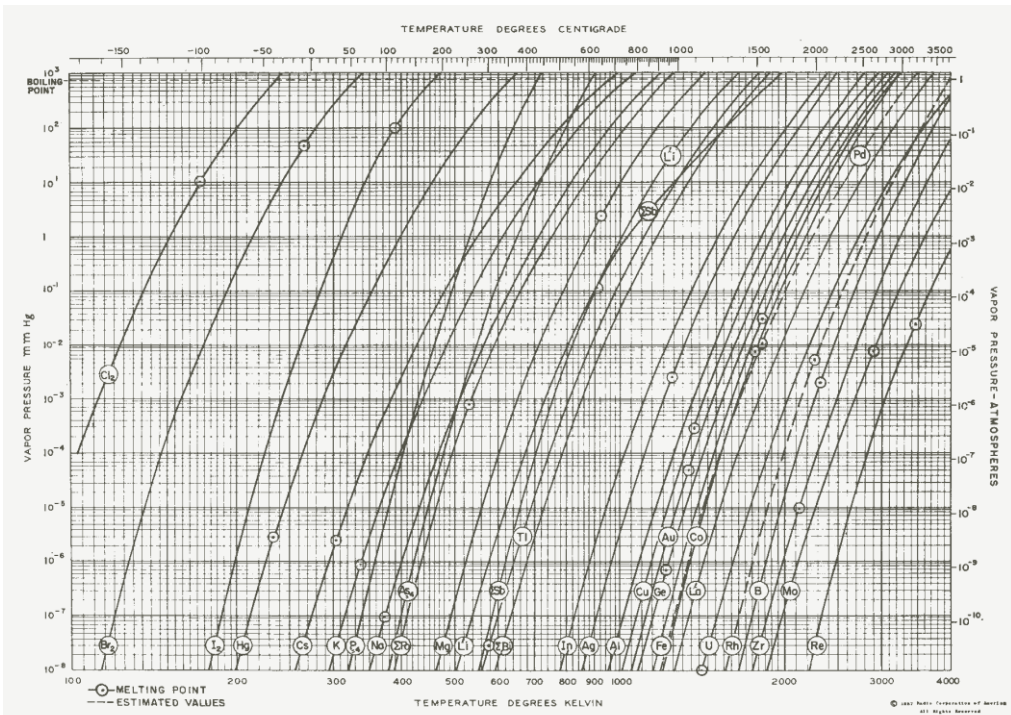


Figure A1(a). Vapor pressure curves for the more common elements. After Honig (Ref. 5:14). (Courtesy RCA)

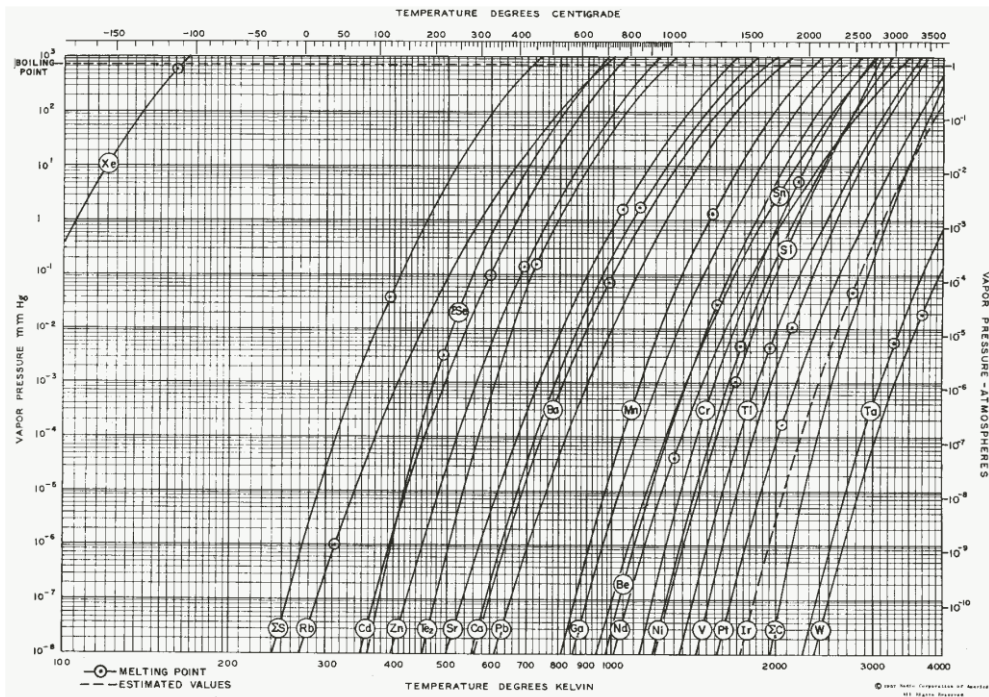


Figure A1(b). Vapor pressure curves for the more common elements (cont.). After Honig (Ref. 5:14).

Figure 37. Vapor pressure of most common elements.[172]

SEM images of as-patterned Si thin films are shown in Figure 38. Figure 38 a) shows sharp contrast between the grid pattern and Si-free region in which the bright squares consist of Si thin films while the relatively dark region are bare sapphire. Figure 38 b) are magnified SEM image of our Si pattern and it is clear that our Si films arrange

regularly upon sapphire substrate and tiny pores can be found within the film, suggesting the film may also aggregate into particles if annealed for a longer time. Figure 38 c) is a further magnified SEM image of our Si patterns and we can tell from the image that as-synthesized Si films are rather thin, for a few nanometers only, and the square edge is pretty flat, suggesting Si atoms coalesce into a film but do not diffuse laterally non-implanting regions during thermal annealing.

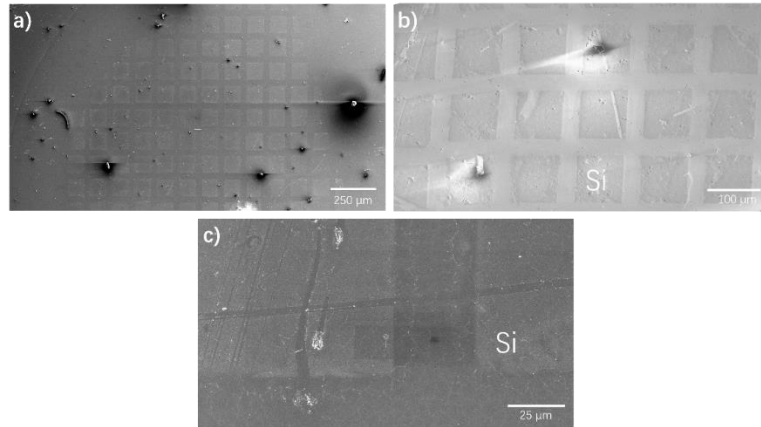


Figure 38. SEM images of patterned Si thin films.

To confirm the existence of Si upon the sapphire surface as well as the film thickness. RBS is conducted and results are shown in Figure 39. Figure 39 a) is the element spectrum where Si, Al signals can be easily found as labeled in the graph respectively. The depth composition diagram is plotted in Figure 39 b) in which the blue, green and orange lines correspond to Si, Al and O signal, respectively. The image conveys information that 1) Si atoms distribute primarily upon the top 3 nm of the surface, indicating a Si film thickness of 3 nm; 2) tiny amount of Si, less than 0.05%, is still observed from 3 nm to 9 nm below the substrate surface, inferring the Si atoms diffuse downwards the substrate to mix with Al and O atoms; 3) huge amounts of O are detected upon the top 9 nm of the surface, indicating our Si film is oxidized to a large extent.

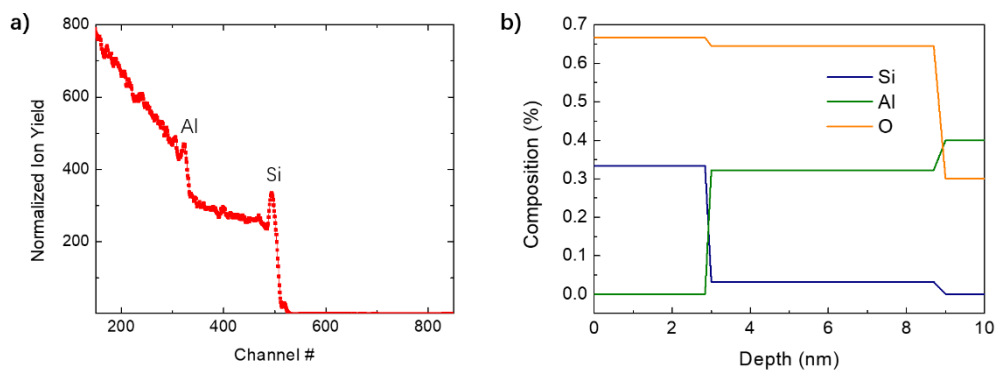


Figure 39. RBS images of as-prepared Si patterns.

To research the crystal structure of our Si thin films AFM images are taken and exhibited in Figure 40. It can be found from Figure 40 a) that our as-synthesized Si films are amorphous composing of discontinuous circular particles with an average particle size calculated to be around 200 nm. Figure 40 b) shows that there are voids between particles and further annealing may exaggerate those voids. From the perspective of Si thin film application, either in solar cells or in semiconductor industries, single crystalline Si film is always more superior than amorphous and polycrystalline Si, therefore, the amorphous film synthesized based on our ion implantation strategy confronts big challenges in film performance and applications. The amorphous structure can be attributed to 1) the high annealing temperature at which Si diffusion proceeds too fast to form a continuous crystal structure and 2) the sapphire substrate used here being energy unfavorable for Si film growth. Therefore, seeking a better annealing plan as well as more energy favorable substrates will be our research topic in the future in order to yield high quality single crystal Si thin films and patterns.

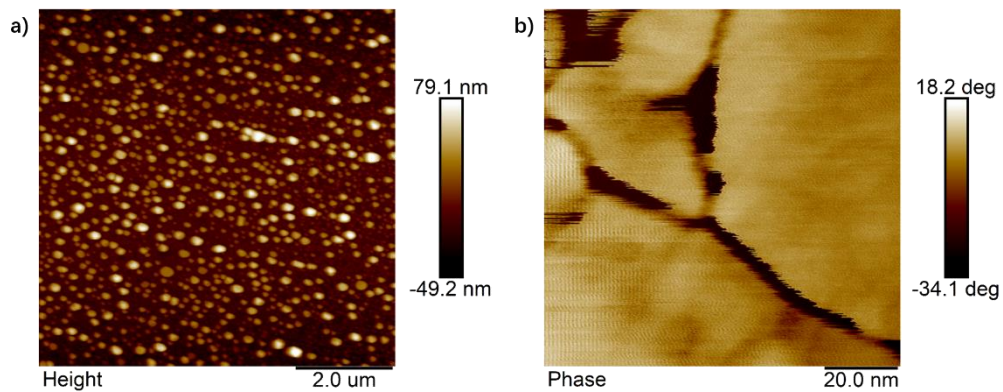


Figure 40. AFM images of Si thin film grains.

TEM and EELS are also conducted to determine the Si atomic arrangement in the film. Figure 41 is the TEM image of the Si/sapphire cross section and EELS map of Si, O and Al are shown in yellow, green and blue color, respectively. Again, from the image we can further conclude that as-deposited Si film is thinner than 10 nm however no crystal structure can be observed from this image. It is also worth mentioning that the sapphire substrate surface fails to be atomically flat due to sputtering-induced surface damage during Ag deposition, which also results in the amorphous Si structure to some extent.

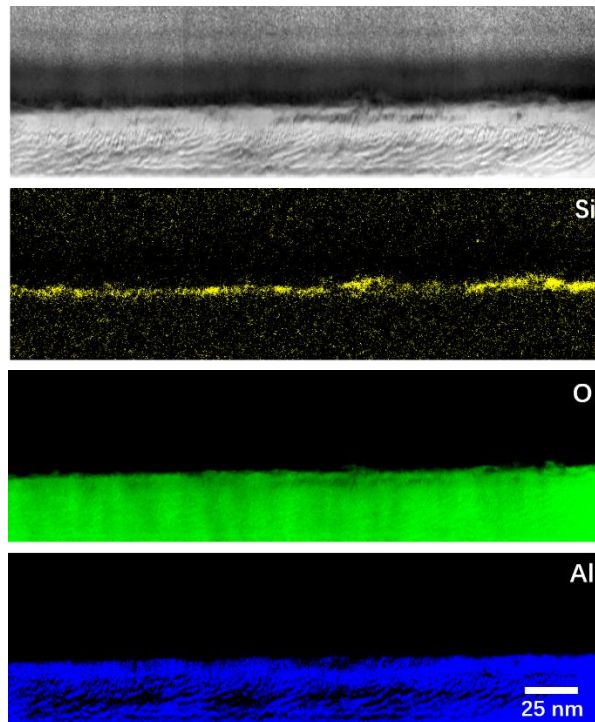


Figure 41. TEM and EELS images of Si/sapphire cross section.

In summary, we introduce here a Si film patterning technique using ion implantation followed by high temperature thermal annealing. SEM, AFM and RBS images demonstrate the existence of Si thin films upon sapphire substrate. By masking certain region of the sample during ion implantation we obtain a Si pattern identical to that of mask, suggesting Si atoms coalesce into a film and do not diffuse laterally towards non-implanting regions during thermal annealing. Unfortunately, only amorphous Si films are prepared in our case, therefore, improving our annealing plan and seeking for more energy favorable substrate to achieve single crystal Si films by ion implantation will be our potential research topic in the future.

#### 4. CONCLUSIONS

To conclude, we introduce a strategy to prevent Ag thin films from dewetting during thermal annealing by ion implantation of a trace amount of external species such as Si and In. Ag thin films either with or without external dopants are characterized by SEM, AFM and AES and the film electrical and optical properties are measured to research the influence of doping ions on film performances. It is found that the film wettability is strongly dependent on the film grain size that is significantly restricted by external dopants during grain growth due to solute drag. Therefore, a grain growth model in existence of solute species and thermodynamic simulation of dewetting are both established to interpret the mechanism of thin film dewetting.

More specifically, two typical phenomena are discovered during grain growth of doped Ag thin films: 1) with the increasing of implanting dose, film grain size decreases significantly and 2) a size limit upon grain growth is observed in doped Ag samples at which grain growth terminates and higher implanting dose contributes to smaller limiting grain size. These two phenomena are attributed to solute drag which is a retarding force originating from the concentration difference of solute atoms in between Ag grains and grain boundaries. Michels established a grain growth model in existence of solute species that described such solute-induced size limit during grain growth. However, this model failed to fit our experimental data points. Therefore, a modified grain growth model is proposed by us here in which we assume the pinning force, i.e. solute drag, is proportional to both the grain size as well as to the solute concentration with a power factor. Curve fitting demonstrates our modified model perfectly suits the grain growth mode of our Ag-Si dopant-film system. The power factor is assumed to be related to the diffusion rate of solute atoms within the film crystals.

AFM characterization enables us to unveil the mechanism of Ag thin film dewetting and it is believed that dewetting initiates at triple grain junctions in the form of pores inside the film; then film grains and pores enlarge simultaneously, exposing subsurfaces to the air and representing the initial intact film evolves into porous film. Consequently, dewetting terminates when grain boundaries disappear and grain surfaces completely spherize. Three phases are defined based on different film morphology during dewetting which are phase I: continuous film, phase II: porous film and phase III: discrete islands, respectively. 3D grain models are created by taking the initial film grains as uniform hexagonal cylinders. Each phase during dewetting can be tracked by the grain wetting angle. Thermodynamic simulation is established according to Miller's model and it is found that after annealing grains in pure Ag films minimize their total surface free energy in phase III: isolated islands while Si-doped Ag films in phase I: continuous film. Combining our modified solute drag model with the thermodynamic simulation we

derive the critical grain diameter to initiate agglomeration of 100 nm thick Ag thin film is 350 nm and the critical Si dose to prevent 100 nm thick Ag thin film from dewetting is  $2.0 \times 10^{13}$  ions per  $\text{cm}^2$ .

Finally, we synthesize Si thin films via ion implantation followed by Ag desorption at a high annealing temperature. As-deposited Si films can be patterned by masking a certain region of the sample during ion implantation and as-achieved pattern has an identical shape as that of mask, suggesting Si atoms reject to diffuse towards non-implanting regions during thermal annealing. Unfortunately, only amorphous Si films are prepared in our case, therefore, improving our annealing plan and seeking for more energy favorable substrate to achieve single crystal Si films by ion implantation strategy will be further researched in the future.

## REFERENCES

- [1] C.V. Thompson, *Solid-State Dewetting of Thin Films*, Annual Review of Materials Research, 42 (2012) 399-434.
- [2] J.J. Rha, J.K. Park, *Stability of the grain configurations of thin films—A model for agglomeration*, Journal of Applied Physics, 82 (1997) 1608-1616.
- [3] A.E.B. Presland, G.L. Price, D.L. Trimm, *Kinetics of hillock and island formation during annealing of thin silver films*, Progress in Surface Science, 3 (1972) 63-96.
- [4] S.-L. Zhang, M. Östling, *Metal Silicides in CMOS Technology: Past, Present, and Future Trends*, Critical Reviews in Solid State and Materials Sciences, 28 (2003) 1-129.
- [5] J.E. Kline, J.P. Leonard, *Suppression of dewetting phenomena during excimer laser melting of thin metal films on SiO<sub>2</sub>*, Thin Solid Films, 488 (2005) 306-313.
- [6] L.R. Zheng, L.S. Hung, S.Q. Feng, P. Revesz, J.W. Mayer, G. Miles, *Interaction of TiSi<sub>2</sub> layers with polycrystalline Si*, Applied Physics Letters, 48 (1986) 767-769.
- [7] T.P. Nolan, R. Sinclair, R. Beyers, *Modeling of agglomeration in polycrystalline thin films: Application to TiSi<sub>2</sub> on a silicon substrate*, Journal of Applied Physics, 71 (1992) 720-724.
- [8] B. Legrand, V. Agache, J.P. Nys, V. Senez, D. Stievenard, *Formation of silicon islands on a silicon on insulator substrate upon thermal annealing*, Applied Physics Letters, 76 (2000) 3271-3273.
- [9] C. Jahan, O. Faynot, L. Tosti, J.M. Hartmann, *Agglomeration control during the selective epitaxial growth of Si raised sources and drains on ultra-thin silicon-on-insulator substrates*, Journal of Crystal Growth, 280 (2005) 530-538.
- [10] Q.Z. Hong, S.Q. Hong, F.M. D'Heurle, J.M.E. Harper, *Thermal stability of silicide on polycrystalline Si*, Thin Solid Films, 253 (1994) 479-484.
- [11] J.P. Gambino, E.G. Colgan, *Silicides and ohmic contacts*, Materials Chemistry and Physics, 52 (1998) 99-146.
- [12] D. Deduytsche, C. Detavernier, R.L. Van Meirhaeghe, C. Lavoie, *High-temperature degradation of NiSi films: Agglomeration versus NiSi<sub>2</sub> nucleation*, Journal of Applied Physics, 98 (2005) 033526.
- [13] L. Xue, Y. Han, *Inhibition of dewetting of thin polymer films*, Progress in Materials Science, 57 (2012) 947-979.
- [14] S. Roy, D. Bandyopadhyay, A. Karim, R. Mukherjee, *Interplay of Substrate Surface Energy and Nanoparticle Concentration in Suppressing Polymer Thin Film Dewetting*, Macromolecules, 48 (2015) 373-382.
- [15] G. Reiter, *DEWETTING OF THIN POLYMER-FILMS*, Physical Review Letters, 68 (1992) 75-78.
- [16] N. Pangpaiboon, N. Traiphol, *Dewetting Suppression of Polystyrene Thin Film Using Titanium Dioxide Nanoparticles*, Key Engineering Materials, 608 (2014) 218-223.

- [17] R. Mukherjee, A. Sharma, *Instability, self-organization and pattern formation in thin soft films*, *Soft Matter*, 11 (2015) 8717-8740.
- [18] R. Xie, A. Karim, J.F. Douglas, C.C. Han, R.A. Weiss, *Spinodal dewetting of thin polymer films*, *Physical Review Letters*, 81 (1998) 1251-1254.
- [19] A. Villares, D.P. Lydon, P.J. Low, B.J. Robinson, G.J. Ashwell, F.M. Royo, P. Cea, *Characterization and Conductivity of Langmuir–Blodgett Films Prepared from an Amine-Substituted Oligo(phenylene ethynylene)*, *Chemistry of Materials*, 20 (2008) 258-264.
- [20] W. Monch, S. Herminghaus, *Elastic instability of rubber films between solid bodies*, *Europhys. Lett.*, 53 (2001) 525-531.
- [21] P.G. Kooijmans, A.A. Smaardijk, *Organic Coatings. Science and Technology. Vol 1: Film Formation, Components, and Appearance*. Z.W. Wicks, Jr., F.N. Jones and S.P. Pappas, John Wiley, Chichester, 1992, xxi + 343 pp £60.00 ISBN 0-471-61406-8, *Recueil des Travaux Chimiques des Pays-Bas*, 112 (1993) 565-565.
- [22] B.D. Gates, Q. Xu, M. Stewart, D. Ryan, C.G. Willson, G.M. Whitesides, *New Approaches to Nanofabrication: Molding, Printing, and Other Techniques*, *Chemical Reviews*, 105 (2005) 1171-1196.
- [23] R. Duncan, *The dawning era of polymer therapeutics*, *Nature Reviews Drug Discovery*, 2 (2003) 347.
- [24] T. Becker, F. Mugele, *Collapse of molecularly thin lubricant layers between elastic substrates*, *J. Phys.-Condes. Matter*, 15 (2003) S321-S330.
- [25] C. Zhang, D. Zhao, D. Gu, H. Kim, T. Ling, Y.K. Wu, L.J. Guo, *An ultrathin, smooth, and low-loss Al-doped Ag film and its application as a transparent electrode in organic photovoltaics*, *Adv Mater*, 26 (2014) 5696-5701.
- [26] C. Zhang, N. Kinsey, L. Chen, C. Ji, M. Xu, M. Ferrera, X. Pan, V.M. Shalaev, A. Boltasseva, L.J. Guo, *High-Performance Doped Silver Films: Overcoming Fundamental Material Limits for Nanophotonic Applications*, *Adv Mater*, 29 (2017).
- [27] J. Mizsei, V. Lantto, *In situ AFM, XRD and Resistivity Studies of the Agglomeration of Sputtered Silver Nanolayers*, *Journal of Nanoparticle Research*, 3 (2001) 271-278.
- [28] K.T. Miller, F.F. Lange, D.B. Marshall, *The instability of polycrystalline thin films: Experiment and theory*, *Journal of Materials Research*, 5 (2011) 151-160.
- [29] C. Manuela Müller, R. Spolenak, *Dewetting of Au and AuPt alloy films: A dewetting zone model*, *Journal of Applied Physics*, 113 (2013) 094301.
- [30] K. Kumar, P. Swaminathan, *Role of silver nanoparticles in the dewetting behavior of copper thin films*, *Thin Solid Films*, 642 (2017) 364-369.
- [31] R.E. Hummel, R.T. DeHoff, S. Matts-Goho, W.M. Goho, *Thermal grooving, thermotransport and electrotransport in doped and undoped thin gold films*, *Thin Solid Films*, 78 (1981) 1-14.
- [32] P. Cao, P. Bai, A.A. Omrani, Y. Xiao, K.L. Meaker, H.Z. Tsai, A. Yan, H.S. Jung, R. Khajeh, G.F. Rodgers, Y. Kim, A.S. Aikawa, M.A. Kolaczowski, Y. Liu, A. Zettl,

- K. Xu, M.F. Crommie, T. Xu, *Preventing Thin Film Dewetting via Graphene Capping*, *Adv Mater*, 29 (2017).
- [33] R.M. Tiggelaar, R.G.R. Sanders, A.W. Groenland, J.G.E. Gardeniers, *Stability of thin platinum films implemented in high-temperature microdevices*, *Sens. Actuator A-Phys.*, 152 (2009) 39-47.
- [34] J.H. Son, G.H. Jung, J.-L. Lee, *Enhancement of light reflectance and thermal stability in Ag-Cu alloy contacts on p-type GaN*, *Applied Physics Letters*, 93 (2008) 012102.
- [35] U. Schmid, *The impact of thermal annealing and adhesion film thickness on the resistivity and the agglomeration behavior of titanium/platinum thin films*, *Journal of Applied Physics*, 103 (2008) 054902.
- [36] J.-Y. Kim, S.-I. Na, G.-Y. Ha, M.-K. Kwon, I.-K. Park, J.-H. Lim, S.-J. Park, M.-H. Kim, D. Choi, K. Min, *Thermally stable and highly reflective AgAl alloy for enhancing light extraction efficiency in GaN light-emitting diodes*, *Applied Physics Letters*, 88 (2006) 043507.
- [37] S.N. Hsiao, S.C. Wu, S.H. Liu, J.L. Tsai, S.K. Chen, Y.C. Chang, H.Y. Lee, *Preventing dewetting during rapid-thermal annealing of FePt films with enhanced L10 ordering by introducing Ag cap-layers*, *Journal of Magnetism and Magnetic Materials*, 394 (2015) 121-125.
- [38] P. Farzinpour, A. Sundar, K.D. Gilroy, Z.E. Eskin, R.A. Hughes, S. Neretina, *Altering the dewetting characteristics of ultrathin gold and silver films using a sacrificial antimony layer*, *Nanotechnology*, 23 (2012) 495604.
- [39] M. Sui, P. Pandey, S. Kunwar, M.Y. Li, Q. Zhang, J. Lee, *Evolution of self-assembled Ag nanostructures on c-plane sapphire by the systematic control of annealing temperature*, *Superlattices and Microstructures*, 100 (2016) 1128-1142.
- [40] O. Malyi, L. Klinger, D.J. Srolovitz, E. Rabkin, *Size and shape evolution of faceted bicrystal nanoparticles of gold on sapphire*, *Acta Materialia*, 59 (2011) 2872-2881.
- [41] S. Kunwar, M. Sui, Q. Zhang, P. Pandey, M.-Y. Li, J. Lee, *Various Silver Nanostructures on Sapphire Using Plasmon Self-Assembly and Dewetting of Thin Films*, *Nano-Micro Letters*, 9 (2016).
- [42] S. Kunwar, M.-Y. Li, P. Pandey, M. Sui, Q. Zhang, J. Lee, *Evolution of morphological and optical properties of self-assembled Ag nanostructures on c-plane sapphire (0001) by the precise control of deposition amount*, *Materials Research Express*, 3 (2016) 125006.
- [43] Y. Kojima, T. Kato, *Nanoparticle formation in Au thin films by electron-beam-induced dewetting*, *Nanotechnology*, 19 (2008) 255605.
- [44] D. Kim, A.L. Giemann, C.V. Thompson, *Solid-state dewetting of patterned thin films*, *Applied Physics Letters*, 95 (2009) 251903.
- [45] D. Gu, C. Zhang, Y.-K. Wu, L.J. Guo, *Ultrasooth and Thermally Stable Silver-Based Thin Films with Subnanometer Roughness by Aluminum Doping*, *ACS Nano*, 8

(2014) 10343-10351.

[46] J. Greiser, D. Müller, P. Müllner, C.V. Thompson, E. Arzt, *Growth of giant grains in silver thin films*, Scripta Materialia, 41 (1999) 709-714.

[47] J. Gong, R. Dai, Z. Wang, Z. Zhang, *Thickness dispersion of surface plasmon of Ag nano-thin films: determination by ellipsometry iterated with transmittance method*, Sci Rep, 5 (2015) 9279.

[48] N. Gazit, L. Klinger, E. Rabkin, *Chemically-induced solid-state dewetting of thin Au films*, Acta Materialia, 129 (2017) 300-311.

[49] W.K. Choi, T.H. Liew, H.G. Chew, F. Zheng, C.V. Thompson, Y. Wang, M.H. Hong, X.D. Wang, L. Li, J. Yun, *A combined top-down and bottom-up approach for precise placement of metal nanoparticles on silicon*, Small, 4 (2008) 330-333.

[50] R.S. Sennett, G.D. Scott, *The Structure of Evaporated Metal Films and Their Optical Properties*, J. Opt. Soc. Am., 40 (1950) 203-211.

[51] J.E. Burke, D. Turnbull, *Recrystallization and grain growth*, Progress in Metal Physics, 3 (1952) 220-292.

[52] J.E. Burke, *Some Factors Affecting the Rate of Grain Growth in Metals*, American Institute of Mining and Metallurgical Engineers, DOI (1949).

[53] T.R. Malow, C.C. Koch, *Grain growth in nanocrystalline iron prepared by mechanical attrition*, Acta Materialia, 45 (1997) 2177-2186.

[54] H. Wang, H. Zhu, *Size evolution of ion beam synthesized Pb nanoparticles in Al*, Nanoscale Research Letters, 9 (2014) 346.

[55] H.S. Zurob, Y. Brechet, G. Purdy, *A model for the competition of precipitation and recrystallization in deformed austenite*, Acta Materialia, 49 (2001) 4183-4190.

[56] L. Slifkin, D. Lazarus, T. Tomizuka, *Self-Diffusion in Pure Polycrystalline Silver*, Journal of Applied Physics, 23 (1952) 1032-1034.

[57] E. Rabkin, *On the grain size dependent solute and particle drag*, Scripta Materialia, 42 (2000) 1199-1206.

[58] H. Natter, M. Schmelzer, M.S. Löffler, C.E. Krill, A. Fitch, R. Hempelmann, *Grain-Growth Kinetics of Nanocrystalline Iron Studied In Situ by Synchrotron Real-Time X-ray Diffraction*, The Journal of Physical Chemistry B, 104 (2000) 2467-2476.

[59] A. Michels, C.E. Krill, H. Ehrhardt, R. Birringer, D.T. Wu, *Modelling the influence of grain-size-dependent solute drag on the kinetics of grain growth in nanocrystalline materials*, Acta Materialia, 47 (1999) 2143-2152.

[60] J.K.L. Lai, C.H. Shek, G.M. Lin, *Grain growth kinetics of nanocrystalline SnO<sub>2</sub> for long-term isothermal annealing*, Scripta Materialia, 49 (2003) 441-446.

[61] E. Jud, C.B. Huwiler, L.J. Gauckler, *Grain Growth of Micron-Sized Grains in Undoped and Cobalt Oxide Doped Ceria Solid Solutions*, Journal of the Ceramic Society of Japan, 114 (2006) 963-969.

[62] C. Hutchinson, H. Zurob, C. Sinclair, Y. Brechet, *The comparative effectiveness of Nb solute and NbC precipitates at impeding grain-boundary motion in Nb steels*, Scripta

Materialia, 59 (2008) 635-637.

[63] R.E. Hoffman, D. Turnbull, *Lattice and Grain Boundary Self-Diffusion in Silver*, Journal of Applied Physics, 22 (1951) 634-639.

[64] J.W. Cahn, *The impurity-drag effect in grain boundary motion*, Acta Metallurgica, 10 (1962) 789-798.

[65] C. Antonione, G.D. Gatta, A. Lucci, G. Riontino, G. Venturello, *The role of substitutional transition elements on recrystallization processes in dilute iron solid solutions*, Acta Metallurgica, 18 (1970) 1169-1180.

[66] H. Sun, C. Deng, *Direct quantification of solute effects on grain boundary motion by atomistic simulations*, Computational Materials Science, 93 (2014) 137-143.

[67] J. Han, P.Q. Mantas, A.M.R. Senos, *Densification and grain growth of Al-doped ZnO*, Journal of Materials Research, 16 (2011) 459-468.

[68] R.J. Brook, *The impurity-drag effect and grain growth kinetics*, Scripta Metallurgica, 2 (1968) 375-378.

[69] H. Zurob, *Effects of Precipitation, Recovery and Recrystallization on the Microstructural Evolution of Microalloyed Austenite*, DOI (2003).

[70] Y. Ogawa, *High Temperature Microscope Observation of the Grain Boundary Migration in Silver under Compression at 500°C*, Transactions of the Japan Institute of Metals, 14 (1973) 22-30.

[71] D. Mclean, *Grain boundaries in metals*, DOI (1957).

[72] A. Lucci, G. Riontino, M.C. Tabasso, M. Tamanim, G. Venturello, *Recrystallization and stored energy of dilute copper solid solutions with substitutional transition elements of the 4th period*, Acta Metallurgica, 26 (1978) 615-622.

[73] C.E. Krill, 3rd, L. Helfen, D. Michels, H. Natter, A. Fitch, O. Masson, R. Birringer, *Size-dependent grain-growth kinetics observed in nanocrystalline Fe*, Phys Rev Lett, 86 (2001) 842-845.

[74] M.P.S.E.D. Hondros, *Grain boundary segregation*, 1973.

[75] M. Hillert, *On the theory of normal and abnormal grain growth*, Acta Metallurgica, 13 (1965) 227-238.

[76] D.M. Duffy, P.W. Tasker, *A calculation of the interaction between impurity ions and grain boundaries in NiO*, Philosophical Magazine A, 50 (2006) 155-169.

[77] A.J. Ardell, *On the coarsening of grain boundary precipitates*, Acta Metallurgica, 20 (1972) 601-609.

[78] K.R. Phaneesh, A. Bhat, P. Mukherjee, K.T. Kashyap, *On the Zener limit of grain growth through 2D Monte Carlo simulation*, Computational Materials Science, 58 (2012) 188-191.

[79] E. Nes, N. Ryum, O. Hunderi, *On the Zener drag*, Acta Metallurgica, 33 (1985) 11-22.

[80] P.A. Manohar, M. Ferry, T. Chandra, *Five Decades of the Zener Equation*, ISIJ International, 38 (1998) 913-924.

- [81] A.G. Aberle, *Thin-film solar cells*, *Thin Solid Films*, 517 (2009) 4706-4710.
- [82] R.B. Bergmann, *Crystalline Si thin-film solar cells: a review*, *Applied Physics A*, 69 (1999) 187-194.
- [83] E.A. Davis, N.F. Mott, *Conduction in non-crystalline systems V. Conductivity, optical absorption and photoconductivity in amorphous semiconductors*, *The Philosophical Magazine: A Journal of Theoretical Experimental and Applied Physics*, 22 (1970) 0903-0922.
- [84] M.A. Green, Y. Hishikawa, E.D. Dunlop, D.H. Levi, J. Hohl-Ebinger, A.W.Y. Ho-Baillie, *Solar cell efficiency tables (version 52)*, *Progress in Photovoltaics: Research and Applications*, 26 (2018) 427-436.
- [85] K. Ishizaki, M. De Zoysa, Y. Tanaka, S.-W. Jeon, S. Noda, *Progress in thin-film silicon solar cells based on photonic-crystal structures*, *Japanese Journal of Applied Physics*, 57 (2018) 060101.
- [86] J. Liu, Y. Yao, S. Xiao, X. Gu, *Review of status developments of high-efficiency crystalline silicon solar cells*, *Journal of Physics D: Applied Physics*, 51 (2018) 123001.
- [87] F. Llopis, I. Tobías, *The role of rear surface in thin silicon solar cells*, *Solar Energy Materials and Solar Cells*, 87 (2005) 481-492.
- [88] J. Lv, M. Xu, S. Lin, X. Shao, X. Zhang, Y. Liu, Y. Wang, Z. Chen, Y. Ma, *Direct-gap semiconducting tri-layer silicene with 29% photovoltaic efficiency*, *Nano Energy*, 51 (2018) 489-495.
- [89] J.-W. Shin, K.-M. Park, J.-E. Kim, S.-Y. Choi, *The Properties of a-Si:H p-i-n Solar Cell by Intrinsic Layer's Thickness*, *Molecular Crystals and Liquid Crystals*, 551 (2011) 257-263.
- [90] M. Yamaguchi, K.-H. Lee, K. Araki, N. Kojima, *A review of recent progress in heterogeneous silicon tandem solar cells*, *Journal of Physics D: Applied Physics*, 51 (2018) 133002.
- [91] J. Yang, A. Banerjee, S. Guha, *Triple-junction amorphous silicon alloy solar cell with 14.6% initial and 13.0% stable conversion efficiencies*, *Applied Physics Letters*, 70 (1997) 2975-2977.
- [92] A. Chutinan, C.W.W. Li, N.P. Kherani, S. Zukotynski, *Wave-optical studies of light trapping in submicrometre-textured ultra-thin crystalline silicon solar cells*, *Journal of Physics D: Applied Physics*, 44 (2011) 262001.
- [93] K. Kumar, K.K.C. Lee, P.R. Herman, J. Nogami, N.P. Kherani, *Femtosecond laser direct hard mask writing for selective facile micron-scale inverted-pyramid patterning of silicon*, *Applied Physics Letters*, 101 (2012) 222106.
- [94] T.D. Lee, A. Ebong, *Thin film solar technologies: a review*, 2015 12th International Conference on High-capacity Optical Networks and Enabling/Emerging Technologies (HONET), 2015, pp. 1-10.
- [95] P. Mahtani, K.R. Leong, B. Jovet, D. Yeghikyan, N.P. Kherani, *High quality amorphous-crystalline silicon heterostructure prepared by grid-biased remote radio-*

- frequency plasma enhanced chemical vapor deposition*, Journal of Non-Crystalline Solids, 358 (2012) 3396-3402.
- [96] H. Mehmood, T. Tauqeer, S. Hussain, *Recent progress in silicon-based solid-state solar cells*, International Journal of Electronics, 105 (2018) 1568-1582.
- [97] P.G. O'Brien, N.P. Kherani, A. Chutinan, G.A. Ozin, S. John, S. Zukotynski, *Silicon Photovoltaics Using Conducting Photonic Crystal Back-Reflectors*, Advanced Materials, 20 (2008) 1577-1582.
- [98] W. Sun, N.P. Kherani, K.D. Hirschman, L.L. Gadeken, P.M. Fauchet, *A Three-Dimensional Porous Silicon p-n Diode for Betavoltaics and Photovoltaics*, Advanced Materials, 17 (2005) 1230-1233.
- [99] M. Ezawa, *Valley-polarized metals and quantum anomalous Hall effect in silicene*, Phys Rev Lett, 109 (2012) 055502.
- [100] C.C. Liu, W. Feng, Y. Yao, *Quantum spin Hall effect in silicene and two-dimensional germanium*, Phys Rev Lett, 107 (2011) 076802.
- [101] P. Vogt, P. De Padova, C. Quaresima, J. Avila, E. Frantzeskakis, M.C. Asensio, A. Resta, B. Ealet, G. Le Lay, *Silicene: compelling experimental evidence for graphenelike two-dimensional silicon*, Phys Rev Lett, 108 (2012) 155501.
- [102] J. Gao, J. Zhao, *Initial geometries, interaction mechanism and high stability of silicene on Ag(111) surface*, Sci Rep, 2 (2012) 861.
- [103] P. Vogt, P. Capiod, M. Berthe, A. Resta, P. De Padova, T. Bruhn, G. Le Lay, B. Grandidier, *Synthesis and electrical conductivity of multilayer silicene*, Applied Physics Letters, 104 (2014) 021602.
- [104] M.R. Tchalala, H. Enriquez, H. Yildirim, A. Kara, A.J. Mayne, G. Dujardin, M.A. Ali, H. Oughaddou, *Atomic and electronic structures of the  $R13.9^\circ$  of silicene sheet on Ag(111)*, Applied Surface Science, 303 (2014) 61-66.
- [105] L. Tao, E. Cinquanta, D. Chiappe, C. Grazianetti, M. Fanciulli, M. Dubey, A. Molle, D. Akinwande, *Silicene field-effect transistors operating at room temperature*, Nat Nanotechnol, 10 (2015) 227-231.
- [106] D. Solonenko, O.D. Gordan, G. Le Lay, D.R.T. Zahn, P. Vogt, *Comprehensive Raman study of epitaxial silicene-related phases on Ag(111)*, Beilstein Journal of Nanotechnology, 8 (2017) 1357-1365.
- [107] P.M. Sheverdyeva, S.K. Mahatha, P. Moras, L. Petaccia, G. Fratesi, G. Onida, C. Carbone, *Electronic States of Silicene Allotropes on Ag(111)*, ACS Nano, 11 (2017) 975-982.
- [108] M. Satta, S. Colonna, R. Flammini, A. Cricenti, F. Ronci, *Silicon Reactivity at the Ag(111) Surface*, Phys Rev Lett, 115 (2015) 026102.
- [109] S. Sadeddine, H. Enriquez, A. Bendounan, P. Kumar Das, I. Vobornik, A. Kara, A.J. Mayne, F. Sirotti, G. Dujardin, H. Oughaddou, *Compelling experimental evidence of a Dirac cone in the electronic structure of a 2D Silicon layer*, Sci Rep, 7 (2017) 44400.

- [110] G. Prévot, R. Bernard, H. Cruguel, Y. Borensztein, *Monitoring Si growth on Ag(111) with scanning tunneling microscopy reveals that silicene structure involves silver atoms*, Applied Physics Letters, 105 (2014) 213106.
- [111] J. Onoda, K. Yabuoshi, H. Miyazaki, Y. Sugimoto, *High-resolution imaging of silicene on an Ag(111) surface by atomic force microscopy*, Physical Review B, 96 (2017).
- [112] Y. Oh, Y. Cho, H. Kwon, J. Lee, I. Jeon, W. Ko, H.W. Kim, J. Ku, G. Kim, H. Suh, S.W. Hwang, *Electronic structure and switching behavior of the metastable silicene domain boundary*, Applied Physics Letters, 110 (2017) 263112.
- [113] A. Molle, C. Grazianetti, D. Chiappe, E. Cinquanta, E. Cianci, G. Tallarida, M. Fanciulli, *Hindering the Oxidation of Silicene with Non-Reactive Encapsulation*, Advanced Functional Materials, 23 (2013) 4340-4344.
- [114] A.J. Mannix, B. Kiraly, B.L. Fisher, M.C. Hersam, N.P. Guisinger, *Silicon Growth at the Two-Dimensional Limit on Ag(111)*, ACS Nano, 8 (2014) 7538-7547.
- [115] Z.-L. Liu, M.-X. Wang, J.-P. Xu, J.-F. Ge, G.L. Lay, P. Vogt, D. Qian, C.-L. Gao, C. Liu, J.-F. Jia, *Various atomic structures of monolayer silicene fabricated on Ag(111)*, New Journal of Physics, 16 (2014) 075006.
- [116] C.L. Lin, R. Arafune, K. Kawahara, M. Kanno, N. Tsukahara, E. Minamitani, Y. Kim, M. Kawai, N. Takagi, *Substrate-induced symmetry breaking in silicene*, Phys Rev Lett, 110 (2013) 076801.
- [117] M. Kurosawa, A. Ohta, M. Araidai, S. Zaima, *Surface-segregated Si and Ge ultrathin films formed by Ag-induced layer exchange process*, Japanese Journal of Applied Physics, 55 (2016) 08NB07.
- [118] H. Jamgotchian, Y. Colignon, N. Hamzaoui, B. Ealet, J.Y. Hoarau, B. Aufray, J.P. Biberian, *Growth of silicene layers on Ag(111): unexpected effect of the substrate temperature*, J Phys Condens Matter, 24 (2012) 172001.
- [119] C. Grazianetti, E. Cinquanta, L. Tao, P. De Padova, C. Quaresima, C. Ottaviani, D. Akinwande, A. Molle, *Silicon Nanosheets: Crossover between Multilayer Silicene and Diamond-like Growth Regime*, ACS Nano, 11 (2017) 3376-3382.
- [120] B. Feng, Z. Ding, S. Meng, Y. Yao, X. He, P. Cheng, L. Chen, K. Wu, *Evidence of silicene in honeycomb structures of silicon on Ag(111)*, Nano Lett, 12 (2012) 3507-3511.
- [121] Y. Du, J. Zhuang, J. Wang, Z. Li, H. Liu, J. Zhao, X. Xu, H. Feng, L. Chen, K. Wu, X. Wang, S.X. Dou, *Quasi-freestanding epitaxial silicene on Ag(111) by oxygen intercalation*, Science Advances, 2 (2016).
- [122] Y. Du, J. Zhuang, H. Liu, X. Xu, S. Eilers, K. Wu, P. Cheng, J. Zhao, X. Pi, K.W. See, G. Peleckis, X. Wang, S.X. Dou, *Tuning the Band Gap in Silicene by Oxidation*, ACS Nano, 8 (2014) 10019-10025.
- [123] A. Curcella, R. Bernard, Y. Borensztein, M. Lazzeri, G. Prevot, *The mechanism for the stabilization and surfactant properties of epitaxial silicene*, Nanoscale, 10 (2018)

2291-2300.

- [124] E. Cinquanta, E. Scalise, D. Chiappe, C. Grazianetti, B. van den Broek, M. Houssa, M. Fanciulli, A. Molle, *Getting through the Nature of Silicene: An  $sp^2$ - $sp^3$  Two-Dimensional Silicon Nanosheet*, The Journal of Physical Chemistry C, 117 (2013) 16719-16724.
- [125] D. Chiappe, C. Grazianetti, G. Tallarida, M. Fanciulli, A. Molle, *Local electronic properties of corrugated silicene phases*, Adv Mater, 24 (2012) 5088-5093.
- [126] L. Chen, C.-C. Liu, B. Feng, X. He, P. Cheng, Z. Ding, S. Meng, Y. Yao, K. Wu, *Evidence for Dirac Fermions in a Honeycomb Lattice Based on Silicon*, Physical Review Letters, 109 (2012) 056804.
- [127] L. Chen, H. Li, B. Feng, Z. Ding, J. Qiu, P. Cheng, K. Wu, S. Meng, *Spontaneous symmetry breaking and dynamic phase transition in monolayer silicene*, Phys Rev Lett, 110 (2013) 085504.
- [128] R. Bernard, Y. Borensztein, H. Cruguel, M. Lazzeri, G. Prévot, *Growth mechanism of silicene on Ag(111) determined by scanning tunneling microscopy measurements and ab initio calculations*, Physical Review B, 92 (2015).
- [129] J. Sone, T. Yamagami, Y. Aoki, K. Nakatsuji, H. Hirayama, *Epitaxial growth of silicene on ultra-thin Ag(111) films*, New Journal of Physics, 16 (2014) 095004.
- [130] G.-W. Lee, H.-D. Chen, D.-S. Lin, *Growth mode and structures of silicene on the Ag(111) surface*, Applied Surface Science, 354 (2015) 187-195.
- [131] P. De Padova, J. Avila, A. Resta, I. Razado-Colambo, C. Quaresima, C. Ottaviani, B. Olivieri, T. Bruhn, P. Vogt, M.C. Asensio, G. Le Lay, *The quasiparticle band dispersion in epitaxial multilayer silicene*, J Phys Condens Matter, 25 (2013) 382202.
- [132] L. Meng, Y. Wang, L. Zhang, S. Du, R. Wu, L. Li, Y. Zhang, G. Li, H. Zhou, W.A. Hofer, H.J. Gao, *Buckled silicene formation on Ir(111)*, Nano Lett, 13 (2013) 685-690.
- [133] L. Huang, Y.F. Zhang, Y.Y. Zhang, W. Xu, Y. Que, E. Li, J.B. Pan, Y.L. Wang, Y. Liu, S.X. Du, S.T. Pantelides, H.J. Gao, *Sequence of Silicon Monolayer Structures Grown on a Ru Surface: from a Herringbone Structure to Silicene*, Nano Lett, 17 (2017) 1161-1166.
- [134] T.G. Gill, A. Fleurence, B. Warner, H. Prüser, R. Friedlein, J.T. Sadowski, C.F. Hirjibehedin, Y. Yamada-Takamura, *Metallic atomically-thin layered silicon epitaxially grown on silicene/ZrB<sub>2</sub>*, 2D Materials, 4 (2017) 021015.
- [135] A. Fleurence, T.G. Gill, R. Friedlein, J.T. Sadowski, K. Aoyagi, M. Copel, R.M. Tromp, C.F. Hirjibehedin, Y. Yamada-Takamura, *Single-domain epitaxial silicene on diboride thin films*, Applied Physics Letters, 108 (2016) 151902.
- [136] A. Fleurence, R. Friedlein, T. Ozaki, H. Kawai, Y. Wang, Y. Yamada-Takamura, *Experimental evidence for epitaxial silicene on diboride thin films*, Phys Rev Lett, 108 (2012) 245501.
- [137] M. De Crescenzi, I. Berbezier, M. Scarselli, P. Castrucci, M. Abbarchi, A. Ronda, F. Jardali, J. Park, H. Vach, *Formation of Silicene Nanosheets on Graphite*, ACS Nano,

- 10 (2016) 11163-11171.
- [138] D. Chiappe, E. Scalise, E. Cinquanta, C. Grazianetti, B. van den Broek, M. Fanciulli, M. Houssa, A. Molle, *Two-dimensional Si nanosheets with local hexagonal structure on a MoS(2) surface*, *Adv Mater*, 26 (2014) 2096-2101.
- [139] T. Aizawa, S. Suehara, S. Otani, *Silicene on Zirconium Carbide (111)*, *The Journal of Physical Chemistry C*, 118 (2014) 23049-23057.
- [140] S.L. Wong, H. Huang, Y. Wang, L. Cao, D. Qi, I. Santoso, W. Chen, A.T.S. Wee, *Quasi-Free-Standing Epitaxial Graphene on SiC (0001) by Fluorine Intercalation from a Molecular Source*, *ACS Nano*, 5 (2011) 7662-7668.
- [141] R. van Bremen, Q. Yao, S. Banerjee, D. Cakir, N. Oncel, H.J.W. Zandvliet, *Intercalation of Si between MoS2 layers*, *Beilstein J Nanotechnol*, 8 (2017) 1952-1960.
- [142] R. Yaokawa, T. Ohsuna, T. Morishita, Y. Hayasaka, M.J. Spencer, H. Nakano, *Monolayer-to-bilayer transformation of silicenes and their structural analysis*, *Nat Commun*, 7 (2016) 10657.
- [143] H.S. Tsai, C.H. Hsiao, C.W. Chen, H. Ouyang, J.H. Liang, *Synthesis of nonepitaxial multilayer silicene assisted by ion implantation*, *Nanoscale*, 8 (2016) 9488-9492.
- [144] J. Liu, Y. Yang, P. Lyu, P. Nachtigall, Y. Xu, *Few-Layer Silicene Nanosheets with Superior Lithium-Storage Properties*, *Adv Mater*, 30 (2018) e1800838.
- [145] S. Lee, K. Kim, K.P. Dhakal, H. Kim, W.S. Yun, J. Lee, H. Cheong, J.H. Ahn, *Thickness-Dependent Phonon Renormalization and Enhanced Raman Scattering in Ultrathin Silicon Nanomembranes*, *Nano Lett*, DOI 10.1021/acs.nanolett.7b03944(2017).
- [146] M.R. Tchalala, M.A. Ali, H. Enriquez, A. Kara, A. Lachgar, S. Yagoubi, E. Foy, E. Vega, A. Bendounan, M.G. Silly, F. Sirotti, S. Nitshe, D. Chaudanson, H. Jamgotchian, B. Aufray, A.J. Mayne, G. Dujardin, H. Oughaddou, *Silicon sheets by redox assisted chemical exfoliation*, *Journal of Physics: Condensed Matter*, 25 (2013) 442001.
- [147] J. Lang, B. Ding, S. Zhang, H. Su, B. Ge, L. Qi, H. Gao, X. Li, Q. Li, H. Wu, *Scalable Synthesis of 2D Si Nanosheets*, *Adv Mater*, DOI 10.1002/adma.201701777(2017).
- [148] X. Zhang, X. Qiu, D. Kong, L. Zhou, Z. Li, X. Li, L. Zhi, *Silicene Flowers: A Dual Stabilized Silicon Building Block for High-Performance Lithium Battery Anodes*, *ACS Nano*, DOI 10.1021/acsnano.7b03942(2017).
- [149] W. Zhang, L. Sun, J.M.V. Nsanzimana, X. Wang, *Lithiation/Delithiation Synthesis of Few Layer Silicene Nanosheets for Rechargeable Li-O2 Batteries*, *Adv Mater*, 30 (2018) e1705523.
- [150] F. Zhang, M. Wang, Z. Wang, K. Han, X. Liu, X. Xu, *Nonlinear absorption properties of silicene nanosheets*, *Nanotechnology*, 29 (2018) 225701.
- [151] R.K. SINNOTT, *Chemical Engineering Design: Chemical Engineering*, Elsevier,

Burlington, 2005.

- [152] G. Rizza, Y. Ramjauny, T. Gacoin, L. Vieille, S. Henry, *Chemically synthesized gold nanoparticles embedded in aSiO<sub>2</sub>matrix: A model system to give insights into nucleation and growth under irradiation*, Physical Review B, 76 (2007).
- [153] S. Garaj, W. Hubbard, J.A. Golovchenko, *Graphene synthesis by ion implantation*, Appl Phys Lett, 97 (2010) 183103.
- [154] L. Baraton, Z.B. He, C.S. Lee, C.S. Cojocaru, M. Châtelet, J.L. Maurice, Y.H. Lee, D. Pribat, *On the mechanisms of precipitation of graphene on nickel thin films*, EPL (Europhysics Letters), 96 (2011) 46003.
- [155] H. Amekura, M. Ohnuma, N. Kishimoto, C. Buchal, S. Mantl, *Fluence-dependent formation of Zn and ZnO nanoparticles by ion implantation and thermal oxidation: An attempt to control nanoparticle size*, Journal of Applied Physics, 104 (2008) 114309.
- [156] D. Ila, E.K. Williams, S. Sarkisov, C.C. Smith, D.B. Poker, D.K. Hensley, *Formation of metallic nanoclusters in silica by ion implantation*, Nuclear Instruments and Methods in Physics Research Section B: Beam Interactions with Materials and Atoms, 141 (1998) 289-293.
- [157] Q. Yu, J. Lian, S. Siriponglert, H. Li, Y.P. Chen, S.-S. Pei, *Graphene segregated on Ni surfaces and transferred to insulators*, Applied Physics Letters, 93 (2008) 113103.
- [158] J.F. Ziegler, *THE STOPPING AND RANGE OF IONS IN SOLIDS*, Ion Implantation Science and Technology (Second Edition), Academic Press 1988, pp. 3-61.
- [159] G. Wang, G. Ding, Y. Zhu, D. Chen, L. Ye, L. Zheng, M. Zhang, Z. Di, S. Liu, *Growth of controlled thickness graphene by ion implantation for field-effect transistor*, Materials Letters, 107 (2013) 170-173.
- [160] H. Li, Y.-X. Shang, Z.-D. Zhang, Z.-S. Wang, R. Zhang, D.-J. Fu, *Preparation of graphene on Cu foils by ion implantation with negative carbon clusters*, Chinese Physics B, 24 (2015) 018502.
- [161] J. Lehnert, D. Spemann, M. Hamza Hatahet, S. Mändl, M. Mensing, A. Finzel, A. Varga, B. Rauschenbach, *Graphene on silicon dioxide via carbon ion implantation in copper with PMMA-free transfer*, Applied Physics Letters, 110 (2017) 233114.
- [162] J.S. Lee, C.W. Jang, J.M. Kim, D.H. Shin, S. Kim, S.-H. Choi, K. Belay, R.G. Elliman, *Graphene synthesis by C implantation into Cu foils*, Carbon, 66 (2014) 267-271.
- [163] J. Kim, G. Lee, J. Kim, *Wafer-scale synthesis of multi-layer graphene by high-temperature carbon ion implantation*, Applied Physics Letters, 107 (2015) 033104.
- [164] G. De Marchi, G. Mattei, P. Mazzoldi, C. Sada, A. Miotello, *Two stages in the kinetics of gold cluster growth in ion-implanted silica during isothermal annealing in oxidizing atmosphere*, Journal of Applied Physics, 92 (2002) 4249-4254.
- [165] Y.A. Agafonov, V.I. Zinenko, O.V. Kononenko, V.V. Saraykin, *Graphene synthesis by cold implantation of carbon recoil atoms*, Technical Physics Letters, 43 (2017) 567-569.

- [166] M.N.J.W. Mayer, *Ion Implantation and Synthesis of Materials*, Springer-Verlag Berlin heidelberg 2006.
- [167] C. Liu, *ALTERNATIVE BINDER PHASES FOR WC CEMENTED CARBIDES*, 2014.
- [168] S.A. Butler, L.L. McDonald, *UNBIASED SYSTEMATIC-SAMPLING PLANS FOR THE LINE-INTERCEPT METHOD*, *Biometrics*, 36 (1980) 737-737.
- [169] L.J.V.d. Pauw, *A Method of Measuring the Resistivity and Hall Coefficient on Lamellae of Arbitrary Shape*, *Philips Technical review*, 20 (1958) 220-223.
- [170] L.X. Chi, N.D. Bassim, *Private Communication from Longxing Chi and Nabil D. Bassim: Department of Materials Science and Engineering, McMaster University*, DOI (2018).
- [171] N. Eustathopoulos, N. Sobczak, A. Passerone, K. Nogi, *Measurement of contact angle and work of adhesion at high temperature*, *Journal of Materials Science*, 40 (2005) 2271-2280.
- [172] C.E. Habermann, A.H. Daane, *Vapor Pressures of the Rare-Earth Metals*, *The Journal of Chemical Physics*, 41 (1964) 2818-2827.